Cell Reports

Article

Activity-dependent localization and dynamics of STIM1 and STIM2 at ER-PM contacts in hippocampal neurons

Graphical abstract

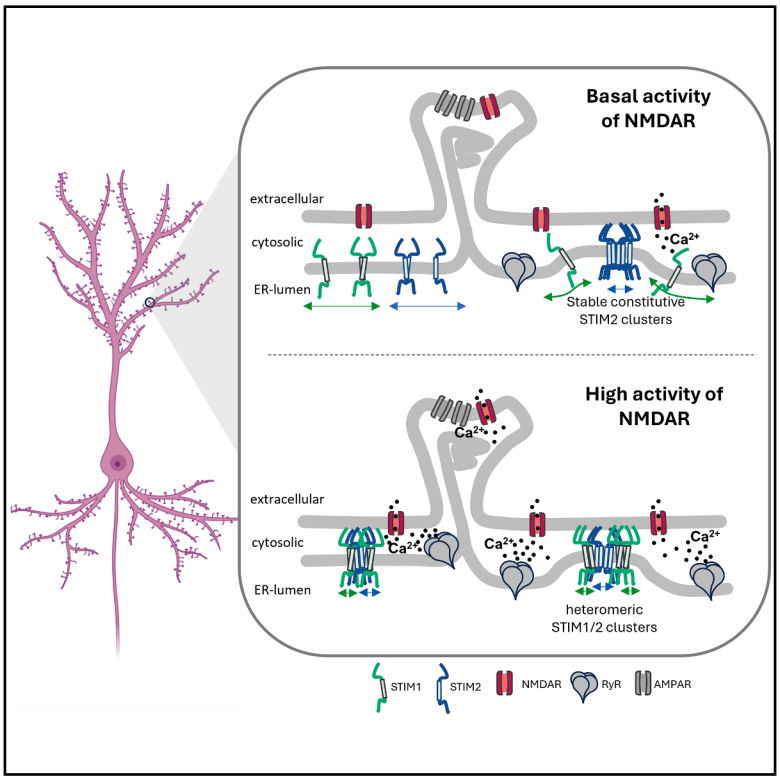

Authors

Arun Chhikara, Filip Maciąg, Nasrin Sorusch, Martin Heine

Correspondence

marthein@uni-mainz.de

In brief

Chhikara et al. show that neuronal STIM proteins are highly dynamic in the ER-plasma membrane but avoid synapses. While STIM2 clusters are modulated by basal NMDAR activity, stimulation of NMDAR triggers co-clustering of STIM1 and STIM2. The clustering of STIM proteins is independent from the activity of $Ca_V1.2$ channels.

Highlights

- STIM1 and STIM2 exhibit variable dynamics in hippocampal neurons and avoid synapses
- STIM2 is constitutively clustered, whereas STIM1 co-clusters with STIM2 upon activation
- ER-PM junctions containing STIMs are distinct from $K_V2.1$ channel-enriched ER-PM junctions
- STIMs do not inhibit $Ca_V1.2$ channels and their dynamics are independent of $Ca_V1.2$ activity

Chhikara et al., 2025, Cell Reports *44*, 116290
October 28, 2025
https://doi.org/10.1016/j.celrep.2025.116290

CellPress

Cell Reports

CellPress
OPEN ACCESS

Article

Activity-dependent localization and dynamics of STIM1 and STIM2 at ER-PM contacts in hippocampal neurons

Arun Chhikara,[1] Filip Maciąg,[1] Nasrin Sorusch,[1] and Martin Heine[1,2,*]
[1]Johannes Gutenberg University Mainz, Institute of Developmental Biology and Neurobiology, AG Functional Neurobiology, Biocenter 1, Hanns-Dieter Hüsch Weg 15, 55128 Mainz, Germany
[2]Lead contact
*Correspondence: marthein@uni-mainz.de
https://doi.org/10.1016/j.celrep.2025.116290

SUMMARY

Stromal interaction molecules (STIMs) are Ca^{2+} sensors within the endoplasmic reticulum (ER) plasma membrane (PM) that contribute to homeostatic functions in neurons. Upon depletion of Ca^{2+} from the ER, STIMs translocate to ER-PM junctions to contact the inner leaflet of the PM. Using single-particle tracking, we characterize the dynamic properties of endogenous STIM1 and STIM2 proteins in hippocampal neurons. STIMs form clusters in the somato-dendritic compartment but only transiently visit synapses. A substantial fraction of STIM2 proteins define ER-PM contacts under resting conditions and is dependent on the constitutive activity of NMDARs. STIM1 proteins are transiently recruited to ER-PM junctions only during strong activation of NMDARs. Activity-dependent confinement of STIM proteins is not influenced by $Ca_V1.2$ channel activity. We propose that STIM proteins fulfill a dominant structural function in neurons by regulating the size and frequency of ER-PM contacts to promote ER-PM communication along dendrites.

INTRODUCTION

ER-PM contacts or junctions are specialized regions where the endoplasmic reticulum (ER) and plasma membrane (PM) come into close proximity (~10 nm in neurons), facilitating interactions between proteins in both membranes.[1] STIM proteins (STIM1 and STIM2 isoforms in mammals) are calcium-sensing proteins in the ER that can directly interact with PM proteins at ER-PM junctions.[2–4] In non-neuronal cells, the interaction between STIM and ORAI proteins opens calcium release-activated channels (CRACs), which are the major components of store-operated calcium entry (SOCE).[5,6] This interaction is triggered by the depletion of calcium from the ER, which is sensed by STIMs, and is an essential mechanism to control intracellular calcium signaling in non-excitable cells.[7–9] In neurons, excitability and local communication are highly dependent on the distribution of voltage-gated calcium channels (VGCCs) and other sources of local calcium signaling. Despite the abundance of STIMs in the nervous system,[7,10,11] the diversity of VGCCs and ligand-gated calcium channels in neurons raises questions about the relevance of SOCE for neuronal function.[12] Neuronal ER-PM junctions cover approximately 10–20% of the total PM area, which is in stark contrast to mere 1–2% in non-excitable cells.[1,13] Neuronal ER-PM junctions are prominent in the soma and dendrite and potentially also within synaptic compartments. About 40% of dendritic spines contain ER-membrane structures, whereas the existence of contacts within the pre-synapse is not supported by electron microscopy (EM)-based reconstructions.[14,15]

Despite the paucity of structural studies for synaptic STIM-ORAI contacts, genetic manipulations of STIMs in neurons suggest that STIMs contribute to synaptic function and connectivity.[16,17] Calcium-induced calcium release (CICR) from intracellular Ca^{2+} stores participates in neurotransmitter release,[18] postsynaptic calcium signaling,[19,20] and stabilization and formation of spines.[14,21] Spatially restricted synaptic activity along dendrites supports the idea of local recruitment of STIMs.[20] In addition to ORAI channels, interactions with AMPA and NMDA receptors are proposed to be modulated by the recruitment of STIMs to ER-PM contacts.[22–28]

As investigated in lymphocytes and other cells, the diffusive organization of STIMs is instructive to understand their function.[29,30] STIMs are dynamic as their activation and interactions with other proteins result in a diffusion trap at ER-PM junctions.[31] Dynamic STIM interactions form transient ER-PM contacts and are modules to regulate local communication between cellular compartments. To investigate the dynamic nature of STIM-mediated contacts in neurons, we employed single-particle tracking (SPT). We focused on predominant STIM splice variants in the hippocampus since STIM1 and STIM2 exhibit a heterogeneous expression in the brain.[32–34]

Our data show that STIMs are mobile throughout the neurons and are more abundant in dendrites than in axons. In dendrites, STIM2 is partially pre-clustered, while STIM1 forms clusters only after ER Ca^{2+} store depletion. NMDAR activation strongly stabilized STIMs, much more than passive ER Ca^{2+} store depletion and independently of $Ca_V1.2$ channel activity. STIMs are confined

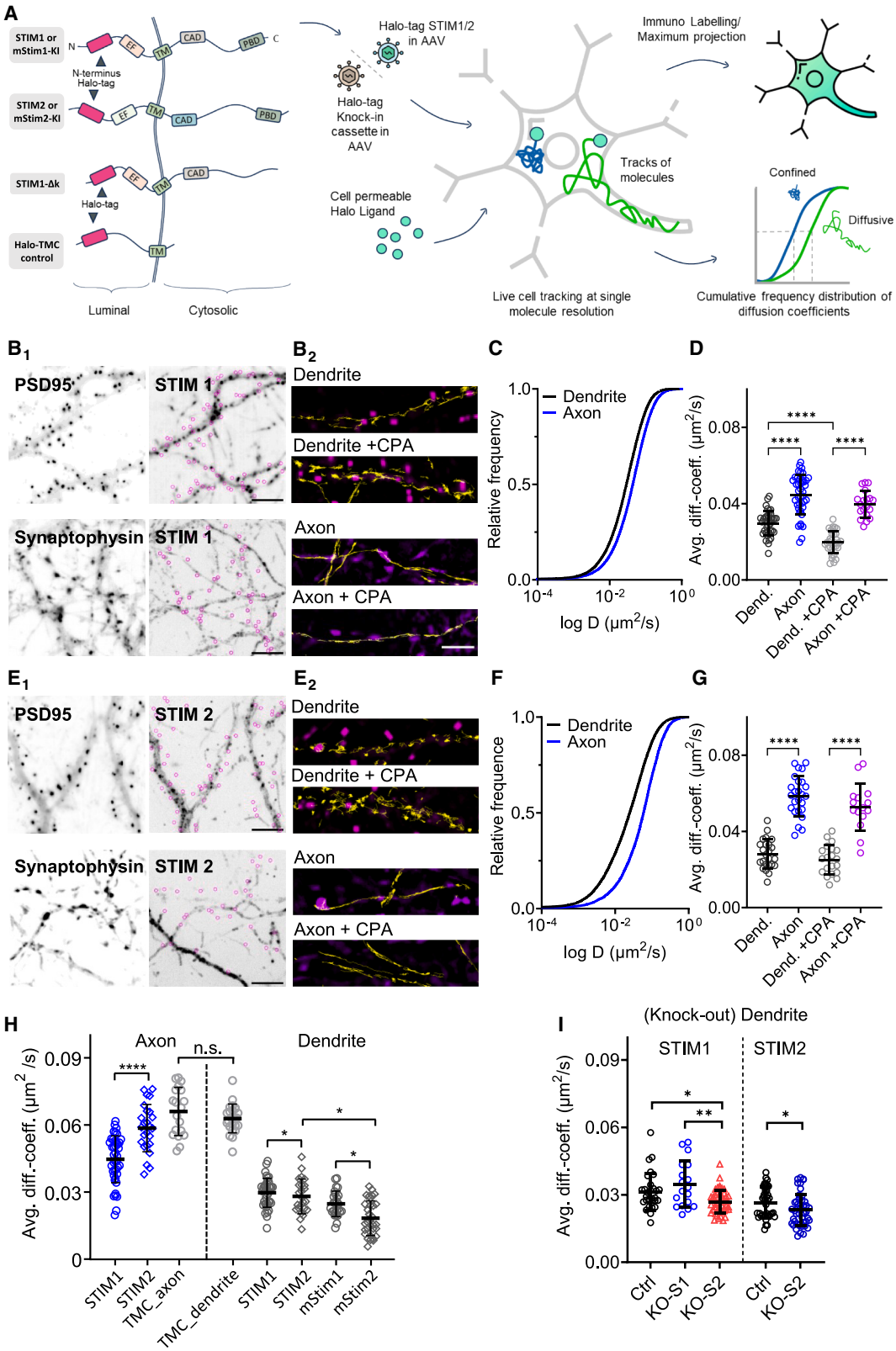

(legend on next page)

at the ER-PM junctions, which are distinct from those populated by voltage-gated K^+ channel ($K_V2.1$) channels. STIMs localize outside presynaptic boutons and postsynaptic spines, which indicate an indirect impact of STIMs on synaptic function.

RESULTS

STIM protein dynamics in dendrites and axons

STIM1 and STIM2 (human isoforms denoted in uppercase, and mouse isoforms as "mStim") both undergo alternative splicing, resulting in variants with distinct functions.[35–37] First, we identified the predominant splice variants of mStims across brain regions using the $2^{\Delta Ct}$ qRT-PCR method (Figure S1). Notably, mStim2 expression was higher than mStim1 in the hippocampus and cerebellum, and mStim1s (NM_009287.5) and mStim2.2 (NM_001081103.2) were the most abundant variants, convergent with other studies.[38] Based on sequence similarities and abundance in hippocampal neurons, human STIM1S (NM_003156.4) and STIM2.2 (NM_020860.4) were chosen as expression constructs. The subcellular distribution of STIMs in mouse hippocampal neurons was examined by three distinct experimental strategies: overexpression, re-expression, and CRISPR-Cas9-mediated endogenous tagging. All three approaches utilized N-terminal Halo-tag label driven by a human synapsin-promotor for neuronal specificity. Constructs were expressed in neurons via recombinant adeno-associated vectors (rAAVs). Real-time tracking of individual STIMs in living neurons was performed by using membrane-permeable Halo-ligands conjugated to the fluorophore JF646. These constructs are referred to as STIM1 and STIM2 unless specified otherwise. The functionality of the constructs was evaluated in HEK293T cells (Figures S2A–S2C). Thereafter, hippocampal neurons at DIV7 were co-transduced with pre- or postsynaptic markers (synaptophysin-GCaMP6, PSD95.FingR-GFP, or PostSyn-TagMA [PSD95], respectively) and Halo-tagged STIMs. Labeling intensity, incubation time, and image acquisition rate were adjusted to gain single-molecule resolution (see STAR Methods, Figure 1A). The dynamics of STIMs were assessed by SPT experiments at DIV14–16 and DIV21–28. Trajectories overlapping with synaptic markers were used to access synaptic localization of STIMs (Figures 1B and 1E).

In control conditions, overexpressed STIM1 was more mobile in axons compared to dendrites (Figures 1C and 1D). Store depletion induced by 20 μM cyclopiazonic acid (CPA) reduced STIM1 diffusion in dendrites; however, it did not change STIM1 mobility in axons (Figure 1D). STIM2 showed more confinement within dendrites (Figure 1E) and higher mobility in axons, even faster than STIM1 (Figures 1F and 1G). STIM2 dynamics in either compartment remained unchanged following CPA-induced store depletion (Figure 1G). In non-excitable cells, STIM2 is often in a pre-clustered state compared to STIM1, even without store depletion.[39] This is reflected in differences between the diffusion coefficients for dendritic STIM2 vs. STIM1 (mean ± SD, $STIM1_{dendrite}$: diff.-coeff. 0.030 ± 0.004 $\mu m^2/s$ vs. $STIM2_{dendrite}$: diff.-coeff. 0.026 ± 0.006 $\mu m^2/s$; Figure 1H). However, in axons, STIM2 is more mobile (mean ± SD, $STIM1_{axon}$: diff.-coeff. 0.044 ± 0.01 $\mu m^2/s$ vs. $STIM2_{axon}$: diff.-coeff. 0.058 ± 0.01 $\mu m^2/s$; Figure 1H), suggesting that not only the local ER calcium concentration influences STIM mobility in neurons.

Several possibilities could influence diffusion properties. First, we probed whether the variation in the tubular architecture of the ER in dendrites and axons[15] impacted the diffusion properties of STIMs.[40] We used a Halo-tagged control construct comprising both the STIM1 signal peptide and the ER transmembrane C terminus of STIM1 (referred to as Halo-TMC; Figure 1A). This ER-membrane construct exhibited similar dynamics in both axons and dendrites without clustering (Figure 1H). Based on these findings, we conclude that differences in ER tubules between dendrites and axons are not a major variable of STIM diffusion. A more obvious reason for the altered mobilities of STIMs could be the variable density of ER-PM junctions in axons and dendrites (Figure S9), the developmental stage of the neuron,[41] or the overexpression of STIMs. Recordings in older neurons (DIV21–28) revealed a significant reduction in the dynamics of STIMs in dendrites and axons (Figure S3; $STIM1_{dendrite,\ DIV14\text{-}16}$: diff.-coeff. 0.030 ± 0.004 $\mu m^2/s$, $STIM1_{dendrite,\ DIV21\text{–}24}$: diff.-coeff. 0.011 ± 0.007 $\mu m^2/s$; $STIM2_{dendrite,\ DIV14\text{–}16}$: diff.-coeff. 0.026 ± 0.006 $\mu m^2/s$, $STIM2_{dendrite,\ DIV21\text{–}24}$: diff.-coeff. 0.006 ± 0.009 $\mu m^2/s$; $STIM1_{axon,\ DIV14\text{–}16}$: diff.-coeff. 0.044 ± 0.01 $\mu m^2/s$, $STIM1_{axon,\ DIV21\text{–}24}$: diff.-coeff. 0.03 ± 0.02 $\mu m^2/s$; $STIM2_{axon,\ DIV14\text{–}16}$: diff.-coeff. 0.058 ± 0.01 $\mu m^2/s$, and $STIM2_{axon,\ DIV21\text{–}24}$: diff.-coeff. 0.028 ± 0.005 $\mu m^2/s$). While

Figure 1. Dynamics of STIMs in neuronal compartments

(A) Representation of the constructs used in this study, highlighting the locations of tags and key domains of STIMs. Also illustrated is the AAV delivery approach and HaloTag labeling methodology employed. The diffusion coefficients derived from MSDs of trajectories are given as cumulative frequency distributions on a logarithmic scale, illustrating the global changes in dynamics.

(B) (B1) Maximum intensity projection of SPT acquisition of overexpressed STIM1, together with post- and presynaptic labeling (PSD95.FingR, synaptophysin-GCaMP, respectively). Magenta circles indicate synaptic locations. (B2) Enlarged view of STIM1 tracks (yellow) within axons and dendrites, juxtaposed against presynaptic and post-synaptic labeling (magenta). Data for control and store-depleted conditions (20 μM CPA) acquired at 37°C.

(C) Cumulative distribution of the diffusion coefficient of STIM1 within axons and dendrites.

(D) Median diffusion coefficient of STIM1 between under control and store-depleted conditions. Each data point represents the median from one acquisition.

(E1–G) Similar experiments as in (B1–D) for STIM2.

(H) Characterization of STIM1 and STIM2 diffusion coefficients in dendrites and axons. Data are from overexpressed STIMs, knockins (mStim_KI), and TMC serving as an ER-targeted control. Only selected statistical comparisons are displayed. See supplemental table showing data for Figure 1.

(I) Re-expression of STIMs following Cre-mediated knockout of endogenous mStim1 (abbreviated as S1) or mStim2 (abbreviated as S2). The terms KO-S1 and KO-S2 refer to the Cre-mediated knockout of mStim1 and mStim2, respectively. rAAV carrying Cre was delivered to neurons on DIV2, while rAAV encoding Halo-STIM1 and Halo-STIM2 was introduced on DIV7. Data acquisition was performed on DIV14–16. Error bars for all figures depict the mean ± SD. Statistical significance is indicated as $^{****}p < 0.0001$, $^{***}p < 0.001$, and $^{*}p < 0.1$. For comparisons between two groups, a parametric unpaired *t* test was used, while multiple groups were analyzed using one-way ANOVA followed by Tukey's multiple comparisons test. Refer to supplemental table showing data for Figure 1 for details.

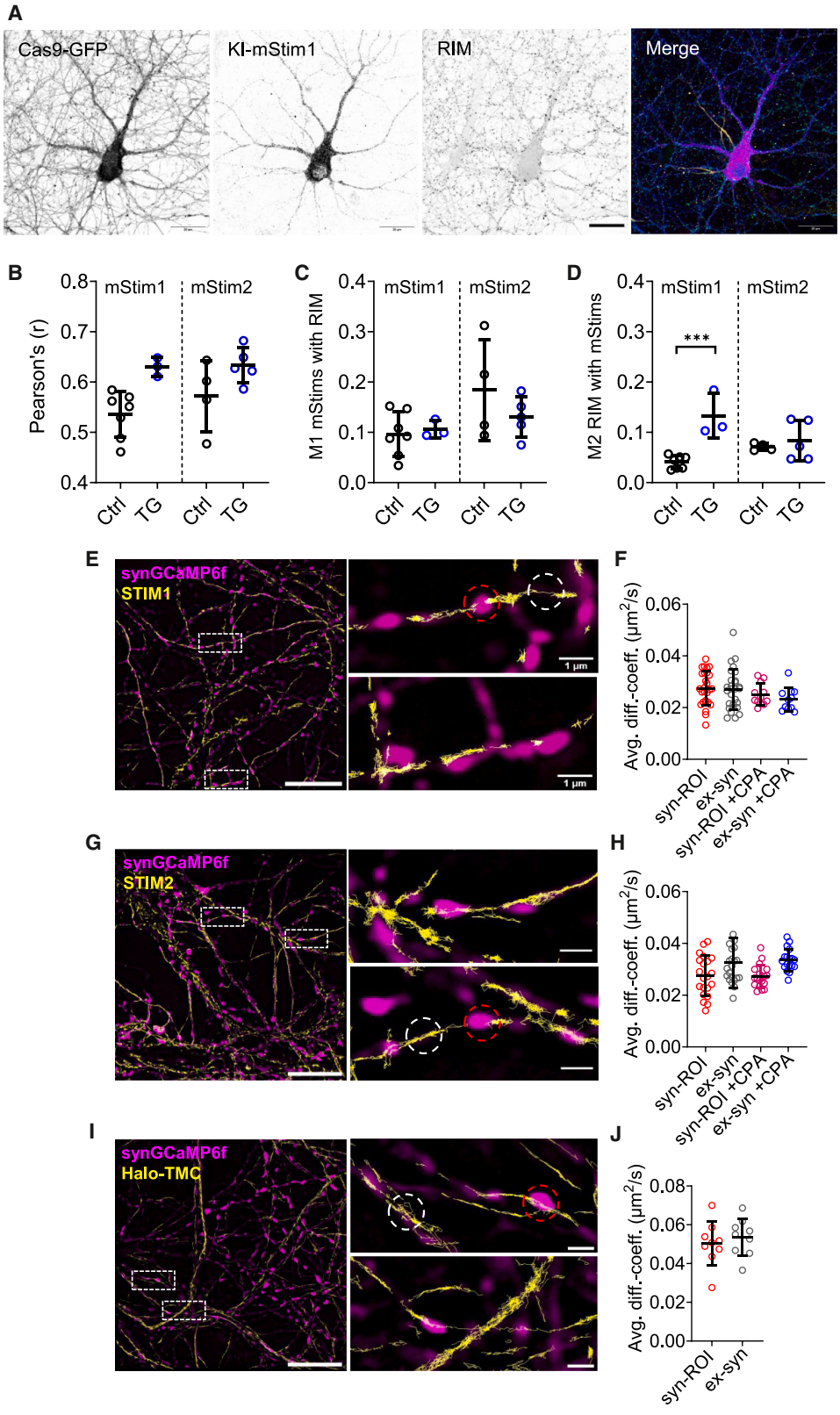

(legend on next page)

tagging does not appear to affect the function of STIMs, indicated by CPA-induced clustering (see above, Figures 1B–1G and S2), overexpression often increases the surface mobility of proteins.[42,43] We performed two control experiments: first, examining the diffusion of overexpressed STIMs in a knockout (KO) background to eliminate the endogenous population of mStim1 or mStim2, and second, tagging and tracking endogenous mStims. The dynamics of STIM1 and STIM2 remained similar after KO and re-expression of the respective isoform, as seen in cultures DIV14–16 (Figure 1I). Interestingly, re-expression of STIM1 in mStim2 KO significantly reduced STIM1 dynamics ($STIM1_{dendrite\ Control}$: diff.-coeff. 0.031 ± 0.008 $\mu m^2/s$, $STIM1_{dendrite\ in\ KO\ of\ mStim2}$: diff.-coeff. 0.026 ± 0.005 $\mu m^2/s$, similar to STIM2 in resting conditions). This suggests that STIM1 compensates for the absence of STIM2 in neurons, similar as also observed in T cells.[44]

To track endogenous mStims, we employed the CRISPR-Cas9-based tagging strategy ORANGE.[45] The Halo-tag was inserted close to the N-terminal position, comparable to overexpression constructs. Infection at DIV3–4 led to a robust expression of tagged mStims in 3–10 neurons per coverslip, corresponding to a success rate of 1‰–5‰ of tagged neurons. Both labeled mStim1 and mStim2 (recorded between DIV14 and DIV21) showed the same trend as seen in overexpressed experiments where STIM1 was more diffusive than STIM2 (Figure 1H). Notably, the overall mobility of endogenous mStims in dendrites was slower. The reasons could be lower expression levels of endogenous proteins compared to overexpression or off-target insertions. However, since both mStim1 and mStim2 were subjected to identical experimental conditions, the observed differences in their dynamics remain reliable and biologically meaningful (Figure 1H). Tracking of endogenous mStims in axons was challenging due to their much lower abundance (mean ± SD: $mStim1_{axon}$: diff.-coeff. 0.023 ± 0.003 $\mu m^2/s$ vs. $mStim2_{axon}$: diff.-coeff. 0.026 ± 0.007 $\mu m^2/s$). Nevertheless, endogenous and overexpression data confirm that isoform-specific mobility differences persist, reinforcing their functional relevance.

STIM proteins are transient visitors in synapses

Previous studies showed a partial colocalization of STIMs in pre- and postsynaptic compartments based on antibody-immunolabeling of endogenous STIMs but reported a variable degree of co-localization.[46–48] The ER does not localize in the presynaptic active zones,[15] but ER tubes exist throughout the axon. Using SPT, we investigated the localization of overexpressed STIMs and immunolabeled Halo-tagged mStim knockins. In knockin neurons, we stained the presynaptic scaffold protein Rab-interacting molecule 1 (RIM1) as the localization signal for presynaptic mStims as well as ankyrin-G to label the initial axon segment (AIS; Figure 2A). Evaluation of Pearson's correlation coefficient revealed a positive correlation between mStims and RIM1 (Figure 2B). However, the Manders' overlap coefficients were low (mean ± SD: M1 mStim1: 0.09 ± 0.04, M1 mStim2: 0.18 ± 0.1, M2 mStim1: 0.04 ± 0.01, M2 mStim2: 0.07 ± 0.01; Figures 2C and 2D), indicating that the signals are not truly colocalized. Depletion of ER Ca^{2+} with CPA or thapsigargin (TG) resulted in a modest increase in the Pearson's coefficient for both mStim1 and mStim2. In contrast, the Manders' overlap coefficients remained largely unchanged, which further prompted us to investigate STIM-synaptic relationship in greater detail using SPT.

Preliminary experiments with electrical field stimulation showed that accumulated calcium signals were larger when SERCA pumps were blocked with CPA, indicating a potential role of STIMs in this process (Figures S2D and S2E). Interestingly SPT imaging with synaptophysin-GCaMP6f as presynaptic label showed STIMs did not accumulate within the presynaptic compartment (Figures $1B_2$, $1E_2$, 2E, and 2G). STIMs occasionally passed through presynaptic membranes, potentially due to the continuous network of ER tubules, which was more evident for the Halo-TMC construct (Figures 2E–2G, 2I, and 2J). To measure changes in the diffusion of STIMs in synapses, we drew regions of interest (ROIs) with a 15-pixel diameter (1.08 μm, corresponding to an area of 0.91 μm^2) around synaptophysin-GCaMP6f spots, as shown in Figures 2E–2G and 2I. These ROIs encompassed not only the synaptic core but also peri-synaptic regions, referred to as syn-ROI in the graphs (Figures 2E, 2G, and 2I). For comparison, identical regions outside synapses were analyzed. Store depletion with CPA did not alter the diffusion properties of either STIM1 or STIM2 in presynaptic and extra-synaptic ROIs, indicating that ER calcium changes do not promote a synaptic recruitment of STIMs (Figures 2F and 2H), despite the functional impact of the ER during strong stimulation of the synapse (Figures S2D and S2E). Immunocytochemical data of knockin neurons also do not support synaptic localization of mStims.

In the postsynaptic compartment, the localization of STIMs near PSD-95 clusters was extremely rare. Maximum projections of SPT movies revealed smooth, tube-like structures for both STIM1 and STIM2. Notably, STIM1 displayed a uniform distribution, while STIM2 exhibited a punctate pattern in dendrites (Figures 3E–3G). In older cultures (DIV21–28), STIMs displayed similar distribution as seen in 2-week-old cultures (Figures S3A

Figure 2. Presynaptic distribution of STIMs

(A) Confocal imaging of knockin Halo-mStim1 in hippocampal cultures, co-labeled with the presynaptic marker RIM. The merged image displays ankyrin-G staining, marked in yellow. Scale bars, 20 μm.

(B) Pearson's correlation coefficients for mStim1/2 with RIM1.

(C) Manders' M1 coefficients (co-localization of mStims with RIM).

(D) Manders' M2 coefficients (co-localization of RIM with mStims) calculated for mStim1 and mStim2 under control and store-depleted conditions (1 μM TG).

(E, G, and I) Visualization of STIM1 (E), STIM2 (G), and Halo-TMC (I) tracks (yellow) in axons co-labeled with synaptophysin-GCaMP. Representative 0.91 μm^2 ROIs are marked as synaptic (red) and extrasynaptic (white). Scale bars, 10 μm for full images, and 2 μm for magnified views.

(F, H, and J) Median diffusion coefficients of STIM1 (F), STIM2 (H), and Halo-TMC (J) plotted under control and store-depleted conditions (20 μM CPA). Error bars indicate the mean ± SD. Statistical significance is indicated as $^{***}p < 0.001$. For comparisons between two groups, an unpaired *t* test was used, while multiple groups were analyzed using one-way ANOVA followed by Tukey's multiple comparisons test. Refer to supplemental table showing data for Figure 2 for details.

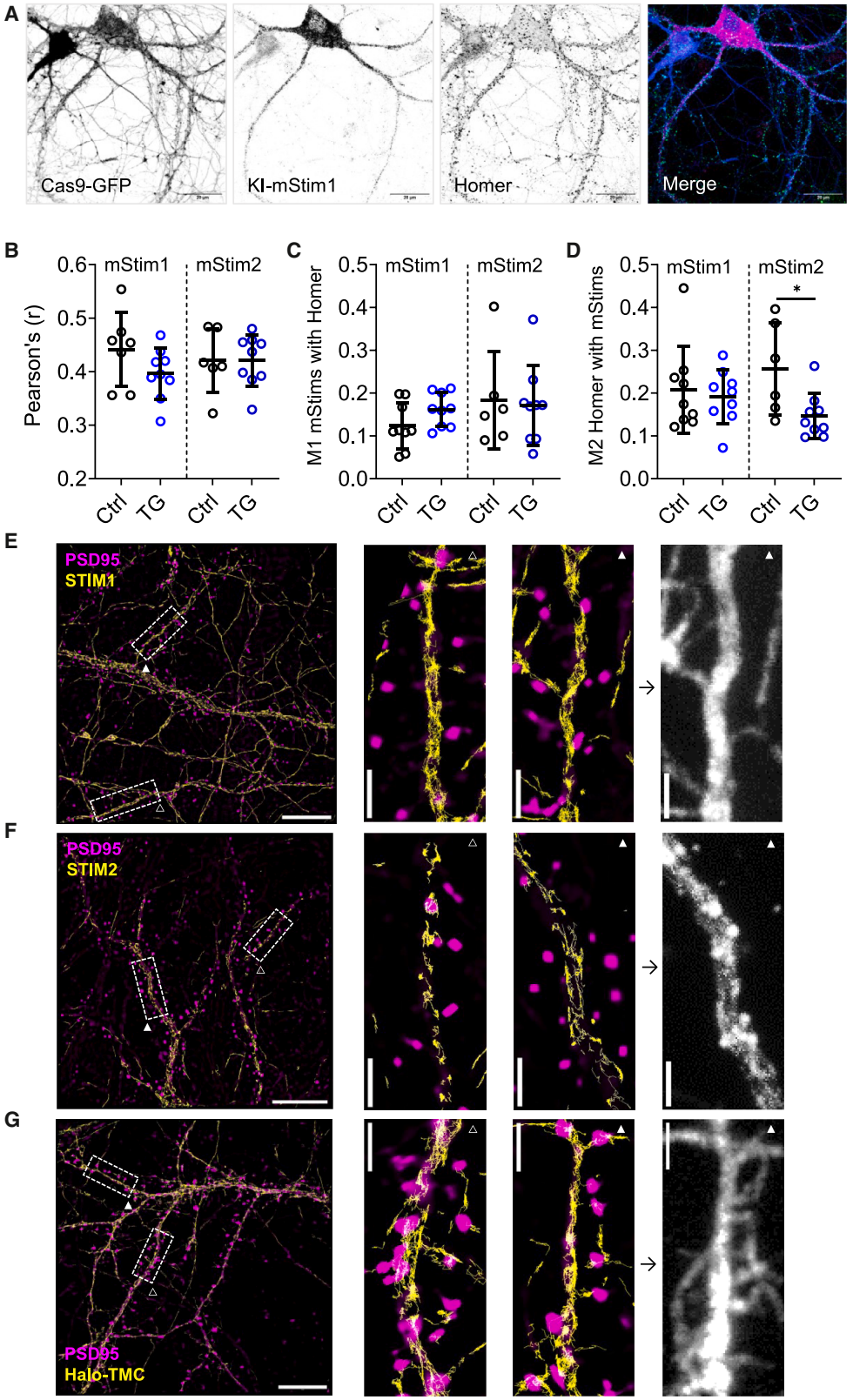

(legend on next page)

and S3B). To assess whether STIMs avoid ER structures like the spine apparatus, we used the Halo-TMC construct as control, which outlined the ER, frequently showing ER structures near PSD-95 spots (Figure 3G). Quantitative analysis indicated that ER visits, visualized by the Halo-TMC, occurred in ~50% of spines, mirroring previously data,[14] while STIMs were rarely detected in the PSD-95 spots (<5%; Figures S3C and S3D).

Immunolabeling of endogenous mStims with the postsynaptic marker Homer (Figure 3A) confirmed our observations. Although Pearson's coefficients revealed a weak positive correlation between Homer and STIMs, the Manders' overlap coefficients were low (Figures 3C and 3D). Both Pearson's and Manders' coefficients remained unchanged after store depletion with TG, suggesting that STIMs are not recruited to postsynaptic spines upon ER Ca^{2+} store depletion (Figures 3B–3D). The results suggest that STIMs are not stabilized within synapses and cluster only along the dendritic shaft.

Chronic and acute changes in neuronal activity alter STIM dynamics in dendrites

While STIMs are not strictly localized to synaptic compartments, we hypothesized that synaptic activity influences ER-PM communication modulating STIM dynamics. STIMs and the ER are critical for homeostatic plasticity through the regulation of calcium signaling.[49,50] In SPT experiments, we first induced chronic changes in neuronal activity. Neurons treated for 24 h with tetrodotoxin (TTX) or bicuculline (BIC) showed significantly altered STIM1 mobility within dendrites. Increased network activity (BIC) restricted STIM1 movement, whereas silencing network activity (TTX) increased STIM1 mobility (Figure S4A). Axonal STIM1 and both axonal and dendritic STIM2 remained unaffected by chronic activity changes (Figures S4B–S4D). To further investigate activity-induced changes in STIM organization, we briefly stimulated glutamate receptors, which induced the clustering of STIMs in dendrites, as reported previously,[19,20] but had no impact on STIM mobility in axons (Figures 4A–4F and S4E–S4H). Due to the lack of changes in the localization or dynamics of STIMs in axons or presynaptic boutons after store depletion or chronic activity changes, we did not further explore STIM dynamics in axons. In addition, the low endogenous expression of mStims in axons further limited our ability to investigate their dynamics (Figure S9).

We hypothesized that calcium influx through NMDARs, which triggers calcium release from the ER via CICR, might be crucial for glutamate-induced STIM clustering. A brief exposure (1 min) of the neurons to 20 μM glutamate caused a robust clustering of dendritic STIM1. Blocking NMDARs using APV (10 μM) prevented the effect of glutamate on STIM1 dynamics (Figures 4A–4C). Maximum projections of STIM1 tracking data showed a uniform signal across the dendrite in control conditions and during the inhibition of NMDARs. Also, the diffusion coefficient of STIM1 was similar under both conditions (Figure 4B). Despite the lower mobility of STIM1s in older cultures (DIV21–28), the activation of NMDARs further reduced the dynamics of STIM1 (median and interquartile range [IQR]: control diff.-coeff.: 0.026 $\mu m^2/s$ IQR 0.014/0.038, 14 ROIs, $N = 2$; NMDA diff.-coeff.: 0.003 $\mu m^2/s$ IQR 0.003/0.004, 7 ROIs, $N = 2$). The contribution of AMPARs and group I metabotropic glutamate receptors was examined as well. Activation of these receptors using specific agonists as AMPA and DHPG, respectively, did not induce changes in STIM1 dynamics in dendrites or axons (Figures S4I–S4L), which is in contrast to former FRAP experiments.[51]

Similar observations were made for STIM2 dynamics in dendrites. Blocking NMDARs prevented glutamate-induced STIM2 clustering in dendrites (Figures 4D–4F). The magnitude of STIM1 diffusion changes appeared to be greater than for STIM2, signifying the broader dynamic range of STIM1 compared to STIM2. Despite their lower mobility, also in older cultures (DIV21–28), STIM2s were further immobilized after the application of NMDA (median and IQR control diff.-coeff.: 0.018 $\mu m^2/s$ IQR 0.016/0.023, 29 ROIs, $N = 2$; NMDA diff.-coeff.: 0.009 $\mu m^2/s$ IQR 0.004/0.017, 9 ROIs, $N = 2$). Next, we investigated if glutamate-mediated clustering of STIMs is facilitated by a tighter association to the PM. This was tested by using STIM1Δk, a mutant lacking the PM-binding PDB domain of STIM1. Upon glutamate treatment, the clustering of STIM1Δk was less robust compared to wild-type STIM1 (Figures 4G and 4H), indicating that the translocation of STIMs to ER-PM junctions contributes to the clustering of STIMs, but it is not the only factor. Differences in the confinement of STIM1 and STIM2 under control conditions (Figures 1H and 1I) suggest that the spontaneous activity of NMDARs might already induce clustering of STIM2. Overnight application of MK-801, an open channel blocker of NMDAR, resulted in a more diffuse distribution of STIM2 (Figure 4I), suggesting that basal NMDAR activity contributes to the confinement of STIM2 in dendrites. Short incubation with MK-801 (<1 h) did not affect the diffusion properties.

We observed that glutamate treatment induced stronger clustering of STIMs compared to passive store depletion by CPA (Figure 4L). The size of endogenous STIM clusters in mStim knockins triggered by NMDA differed from those clusters induced by TG-induced SERCA inactivation. Both mStim1 and mStim2 clusters were larger following NMDA treatment compared to TG treatment (Figures 4J and 4K). Ryanodine-induced depletion of ER stores via the activation of ryanodine receptors (RyRs) also resulted in less pronounced STIM clustering compared to NMDA or glutamate treatment

Figure 3. Post-synaptic distribution of STIMs

(A) Confocal imaging of knockin Halo-mStim1 in hippocampal cultures, co-labeled with the post-synaptic marker Homer. Scale bars, 20 μm.

(B–D) Pearson's correlation coefficients of mStims with Homer (B), Manders' M1 coefficients (co-localization of mStims with Homer) (C), and Manders' M2 coefficients (co-localization of Homer with mStims) (D). Error bars indicate the mean ± SD.

(E–G) Visualization of Halo-STIM1 (E), STIM2 (F), and Halo-TMC (G) tracks (yellow) in dendrites co-labeled with PSD-95. The grayscale images represent maximum projections of SPT movies without synaptic labels in magnified dendritic sections. Scale bars, 10 μm (large images) and 2 μm (magnified views). Error bars indicate the mean ± SD. For statistical significance an unpaired *t* test was used indicated as $*p < 0.1$. Refer to supplemental table showing data for Figure 3 for details.

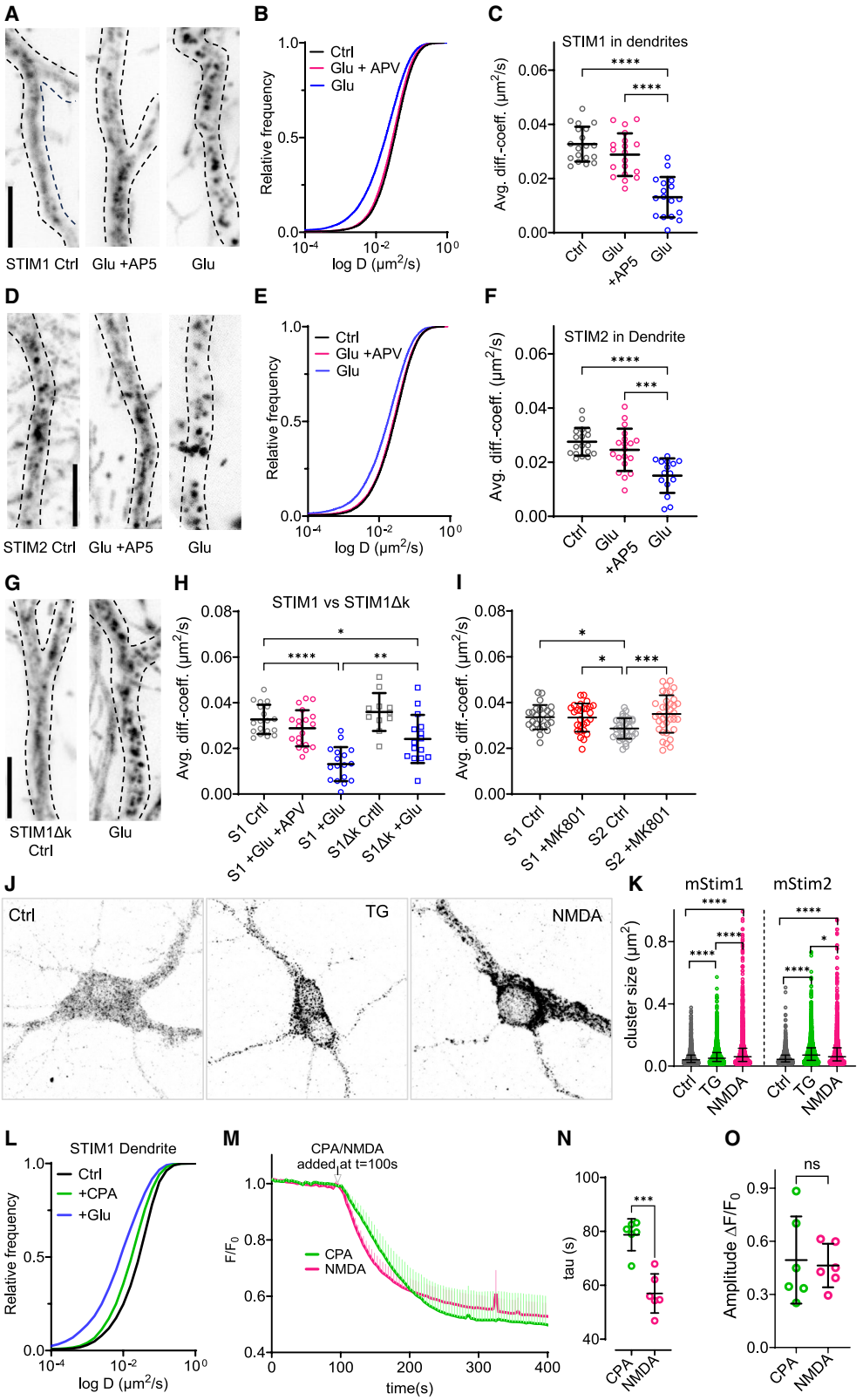

(legend on next page)

(Figures S5A and S5B). According to other studies on STIM function, the degree of store depletion, irrespective of the depletion method, should correlate with the extent of STIM clustering and activation.[52] To validate this, we compared store depletion induced by NMDA and CPA using ER-GCaMP Ca^{2+} imaging. Both treatments resulted in similar final depletion levels (Figures 4M and 4O). However, the rate of ER Ca^{2+} depletion was faster upon NMDA treatment compared to CPA (Figures 4M and 4N).

Glutamate-induced STIM clustering is not dependent on the activity of $Ca_V1.2$

Apart from the classical STIM-ORAI interaction, several studies reported a functional relationship between STIMs and $Ca_V1.2$ channels. Both STIM isoforms have been shown to directly inhibit $Ca_V1.2$ channel activity.[3,53] Direct glutamate uncaging experiments revealed that STIMs, particularly STIM1, regulate $Ca_V1.2$ channel activity.[20] By performing somatic calcium current measurements, local dendritic calcium imaging, and shRNAi-mediated suppression of STIM1, the following signaling pathway was proposed: NMDAR activation, along with AMPAR-induced depolarization, opens synaptic and peri-synaptic $Ca_V1.2$ channels, which subsequently triggers CICR and STIM1 clustering. STIM1 transiently clusters following glutamate application and inhibits $Ca_V1.2$ channels, thereby preventing excessive Ca^{2+} influx into the postsynaptic compartment. Notably, direct $Ca_V1.2$ inhibition was shown to reduce STIM1 clustering.[20] Thus, blocking $Ca_V1.2$ channels should influence glutamate-induced STIM clustering. We tracked STIMs following NMDA treatment in the presence of the $Ca_V1.2$ channel blocker nimodipine (nim). However, nim did not inhibit STIM1 cluster formation (Figures 5A–5C). Activation of $Ca_V1.2$ channels with BayK had no effect on STIM1 mobility, either, in contrast to glutamate (Figures S4M–S4O). Furthermore, the analysis of STIM1 mobility revealed no difference between nim-pretreated neurons and control neurons (Figure 5B). This suggests that NMDA-mediated STIM1 clustering occurs independently of $Ca_V1.2$ channel activation. We further investigated the effect of $Ca_V1.2$ channel blockade on ER Ca^{2+}. Nim did not alter the kinetics or magnitude of ER Ca^{2+} efflux triggered by NMDA (Figure 5D), suggesting no major impact of $Ca_V1.2$ channel activity on NMDAR-induced changes in ER calcium.

To evaluate the specificity of NMDAR-induced STIM1 clustering, we explored the duration of STIM1 clustering after the washout of NMDA. NMDA-triggered STIM1 clustering persisted for approximately 5 min. The dynamics of STIM1 returned to basal level within the next 10 min (Figures 5E–5G). This time (5–10 min) aligns with reported effects of glutamate on ER calcium levels.[20] We replicated the time course in nim-pretreated neurons followed by NMDA exposure. Like the NMDA-only treatment, STIM1 clustered for 5 min before reverting to normal diffusion by 10 min (Figures 5H and 5I). These experiments confirm the transient nature of STIM1 clustering, as reported,[20] but further emphasize that STIM1 clustering is independent of $Ca_V1.2$ channel activity.

Similar results were obtained for STIM2. Nim did not prevent the robust clustering of STIM2 triggered by NMDA (Figures 5J–5L). STIM2 clusters formed upon NMDA exposure, and the clustering pattern remained unchanged when $Ca_V1.2$ channels were blocked alongside NMDA activation (Figure 5L). Analysis of STIM2 dynamics under both conditions showed no significant differences, confirming that nim had no effect on NMDA-mediated clustering of either STIM1 or STIM2 (Figures 5C and 5L). Similar to STIM1, the NMDA effect was reversable after washout (Figure 5M). These experiments suggest that $Ca_V1.2$ channels are not crucial for NMDA-induced clustering of either STIM1 or STIM2.

The clustering of a subpopulation of STIM2 proteins under control conditions could indicate that a fraction of ER-PM junctions composed of STIM2-ORAI may exist to support the replenishment of ER calcium during neuronal network activity. Using Fura-2 imaging, we measured cytosolic calcium in control and mStim KO neurons. Neurons were infected with rAAVs to express Cre or a mutated Cre (ΔCre). Both AAVs expressed a bicistronic td-tomato reporter signal (Figures S6A–S6H) to identify infected neurons. KO of either mStim1 or mStim2 did not affect basal cytosolic Ca^{2+} concentration, which suggests that SOCE is not a critical determinant of resting cytoplasmic Ca^{2+} in eurons (Figures 5N–5Q). Next, we depolarized the neuronal membrane by addition of KCl (50 mM). There was no impact

Figure 4. Glutamate-induced clustering of STIMs depends on NMDA signaling and neuronal activity

(A) Representative maximum projections of Halo-STIM1 movies for conditions as indicated.

(B) Cumulative frequency distribution of STIM1 diffusion coefficients under control (black), glutamate + APV (red), and glutamate (blue).

(C) Comparison of median diffusion coefficients for STIM1. Each dot represents the median from one acquisition. For statistics, see supplemental table showing data for Figure 4.

(D–F) Similar data for STIM2.

(G) Maximum projection images of STIM1ΔK under control conditions and after treatment with glutamate.

(H) Median diffusion coefficients of STIM1ΔK, including comparisons with STIM1.

(I) Statistical analysis and comparision of diffusion coefficients of both STIM1 (S1) and STIM2 (S2) to 24-h MK-801 treatment.

(J) Immunostaining of endogenously labeled mStim1 in Cas9 neurons; shown are mStim1-positive neurons under control conditions and after the application of TG or NMDA.

(K) Cluster-size quantification of mStims under control, TG, and NMDA treatments, analyzed from 4 to 5 cells per condition.

(L) Cumulative frequency distribution of diffusion coefficients for STIM1 under control conditions and after the application of glutamate (20 μM) or CPA (20 μM).

(M) ER-GCaMP Ca^{2+} imaging in hippocampal neurons stimulated with CPA or NMDA to induce Ca^{2+} release from ER.

(N) Quantification of ER Ca^{2+} release kinetics by fitting a monoexponential function to the decay of ER-GCamp fluorescence.

(O) Amplitude of ER Ca^{2+} release quantified between baseline and plateau after the application of CPA or NMDA. Error bars represent the mean ± SD. Statistical significance is indicated as $^{****}p < 0.0001$, $^{***}p < 0.001$, and $^{*}p < 0.1$. For comparisons between two groups, a parametric unpaired *t* test was used, while multiple groups were analyzed using one-way ANOVA followed by Tukey's multiple comparisons test. Refer to supplemental table showing data for Figure 4 for details.

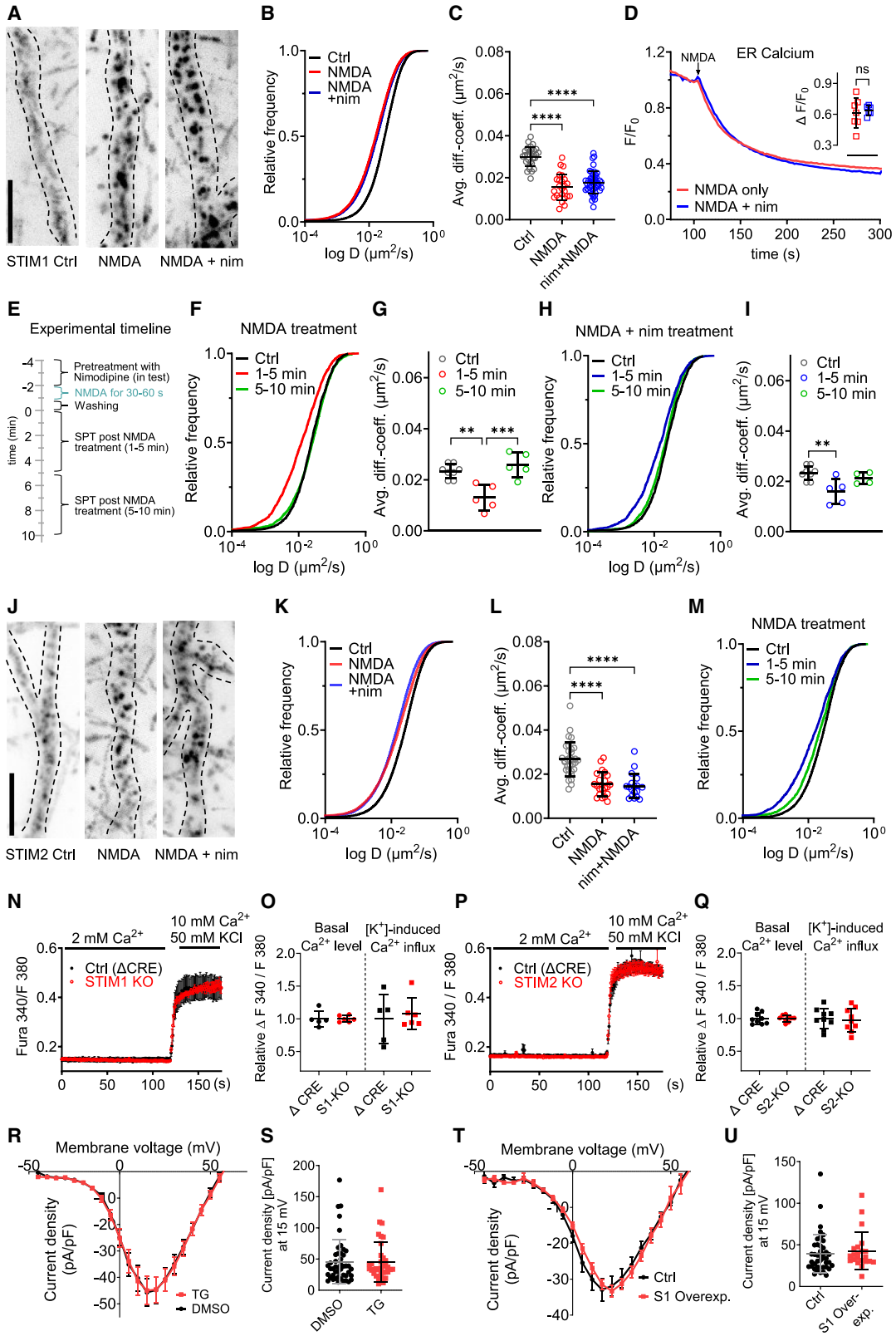

(legend on next page)

on the induced calcium transients in mStim1 or mStim2 KOs (Figures 5N–5Q). The reduction in mStim-mediated inhibition of $Ca_V1.2$ channels should result in a higher amplitude of depolarization-induced Ca^{2+} transients. However, KO of mStim1 or mStim2 had no influence. These experiments do not support a direct impact of STIMs on the activity of $Ca_V1.2$ channels in mouse hippocampal neurons. We further used whole-cell patch-clamp recordings in HEK cells expressing $Ca_V1.2$ channels to probe the interaction between $Ca_V1.2$ and STIM1s. Neither the activation of endogenous STIM1 by ER Ca^{2+} store depletion nor the overexpression of EYFP-STIM1 altered the current amplitude (Figures 5R–5U). Altogether, SPT experiments, imaging of cytosolic and ER Ca^{2+} signals, and patch-clamp data argue against a direct coupling of STIMs with $Ca_V1.2$ channels.

Neuronal ER-PM junctions are populated by clusters of $K_V2.1$ channels containing $Ca_V1.2$ channels in the soma and proximal dendrites, and a subpopulation of clustered STIM2s contributes to these clusters.[54–56] However, the lack of interactions between $Ca_V1.2$ channels and STIMs hints that STIMs form separate ER-PM contacts, which are modulated in their dimensions (Figure 4K) by the activation of NMDAR.

STIMs are not confined to one type of contact

Immunolabeling revealed that the cluster size and morphology of mStim1 (Figure 6A) and mStim2 clusters (Figure S7A) were markedly different from $K_V2.1$ clusters, which typically covered a larger area than mStim clusters. We checked whether mStim and $K_V2.1$ intensities were correlated and to which extent their clusters overlap. Quantification of colocalization in both control and store-depleted conditions revealed low Manders' coefficient values (Figures 6C, 6D, and S7A). Similarly, Pearson's coefficient showed a weak positive correlation between $K_V2.1$ and mStim signals that did not change upon ER Ca^{2+} depletion (Figure 6B; Figure S7). As mStim immunolabeling always possesses significant background noise, we further validated the colocalization of overexpressed Halo-STIM2 with $K_V2.1$ channel clusters, confirming a weak overlap of the two signals (Figure S7B). Interestingly, immunolabeling the endogenous population of mStim2 showed an inverse correlation between endogenous mStim2 and $K_V2.1$ expression levels. Cells with high $K_V2.1$ levels displayed lower mStim2 levels (Figure S8A). Repeating these experiments in primary cultures from a GAD67-GFP positive mouse line revealed that particularly GABAergic neurons exhibited higher $K_V2.1$ expression and lower levels of mStim2 expression (Figures S8B–S8E). Encouraged by this finding, we investigated whether there is indeed a direct correlation between mStim2 and $K_V2.1$ to regulate each other's expression. However, mStim2 knockdown did not change $K_V2.1$ expression or the morphology of clusters (Figure S8F).

Previous studies showed that $K_V2.1$ clusters disassemble upon glutamate treatment.[57,58] We confirmed this by showing that the number of $K_V2.1$ clusters decreases after neurons have been exposed to glutamate. The opposite was observed for STIMs, where glutamate stimulation caused a robust clustering of STIMs (Figures 4A–4F, 4J, 4K, S8G, and S8H). The weak colocalization and opposing responses to glutamate imply that $K_V2.1$ channels and STIMs form distinct ER-PM junctions that differ in size and sensitivity to glutamate.

Using an ER-PM junction marker called MAPPER,[59] we strengthened this interpretation. Surface labeling of $K_V2.1$ channels together with MAPPER showed a different morphology of clusters. $K_V2.1$ channel clusters were larger than MAPPER clusters (Figures 6E–6G). The average $K_V2.1$ channel cluster area was approximately 2.7 μm^2, whereas MAPPER clusters' area was about 0.5 μm^2 (Figure 6G). Both populations showed only a partial overlap (Figure 6F). Overall, MAPPER clusters were abundant along the cell soma and dendrites but not in axons (Figures S9A–S9C). A strong decrease in the MAPPER signal intensity was observed along the AIS, as compared with the somato-dendritic compartment (Figure S9B). Similar, the density of endogenously labeled mStims differed significantly between dendrites and axons (Figure S9C). Co-expression of STIMs and MAPPER confirmed that under control conditions, STIM2, but not STIM1, is confined

Figure 5. Contribution of $Ca_V1.2$ channels to NMDA-induced clustering of STIMs

(A) Maximum intensity projections from STIM1 movies for control conditions, after NMDA, and NMDA + nimodipine treatment. For nimodipine treatment, cells were pre-incubated with 50 μM nimodipine (nim) for 3 min prior to NMDA activation.

(B) Cumulative frequency distribution of STIM1 diffusion coefficients for treatments as indicated.

(C) Comparison of median diffusion coefficients for STIM1. Each dot represents median diffusion coefficients from one single acquisition. For statistics, see supplemental table showing data for Figure 5.

(D) ER-GCaMP-150 calcium imaging, NMDA was added as indicated for both control and nimodipine pre-treated conditions (see STAR Methods).

(E) Experimental timeline for assessing the temporal dynamics of STIMs following NMDA treatment.

(F and H) Cumulative distribution of STIM1 diffusion coefficients for conditions as indicated.

(G and I) Median diffusion coefficients for corresponding conditions. Control recordings primarily included data from the first 1–5 min of acquisition. For NMDA- and nimodipine + NMDA-treated cells, recordings were separated and plotted as two distinct time intervals: 1–5 min and 5–10 min post-NMDA treatment.

(J) Representative maximum projections from STIM2 movies for control conditions, after NMDA, and NMDA + nimodipine treatment.

(K and L) (K) Cumulative frequency distribution of STIM2 diffusion coefficients for treatments as indicated. (L) Comparison of median diffusion coefficients for STIM2. Each dot represents one ROI. For statistics, see supplemental table showing data for Figure 5.

(M) Cumulative frequency distribution of STIM2 diffusion coefficients at control and 1–5 min or 5–10 min post-NMDA treatment.

(N–Q) Cytosolic calcium levels were measured in hippocampal neurons loaded with Fura-2 under control conditions or after KD of Stim1 (N and O) or Stim2 (P and Q). Data were collected from neurons at DIV14–16.

(R–U) Whole-cell patch-clamp recordings from HEK293T cells stably expressing L-type 1.2 calcium channels (see STAR Methods). (R and S) IV curve of $Ca_V1.2$ calcium currents following store depletion by 1 μM TG or vehicle control (DMSO). (T and U) IV curve of $Ca_V1.2$ calcium currents in cells overexpressing EYFP-STIM1 in comparison to control. Refer to supplementary table Figure 5 for p values and data quantities. Error bars indicate the mean ± SD. Statistical significance is indicated as $^{****}p < 0.0001$, $^{***}p < 0.001$, and $^{*}p < 0.1$. For comparisons between two groups, a parametric unpaired t test was used, while multiple groups were analyzed using one-way ANOVA followed by Tukey's multiple comparisons test. Refer to supplemental table showing data for Figure 5 for details.

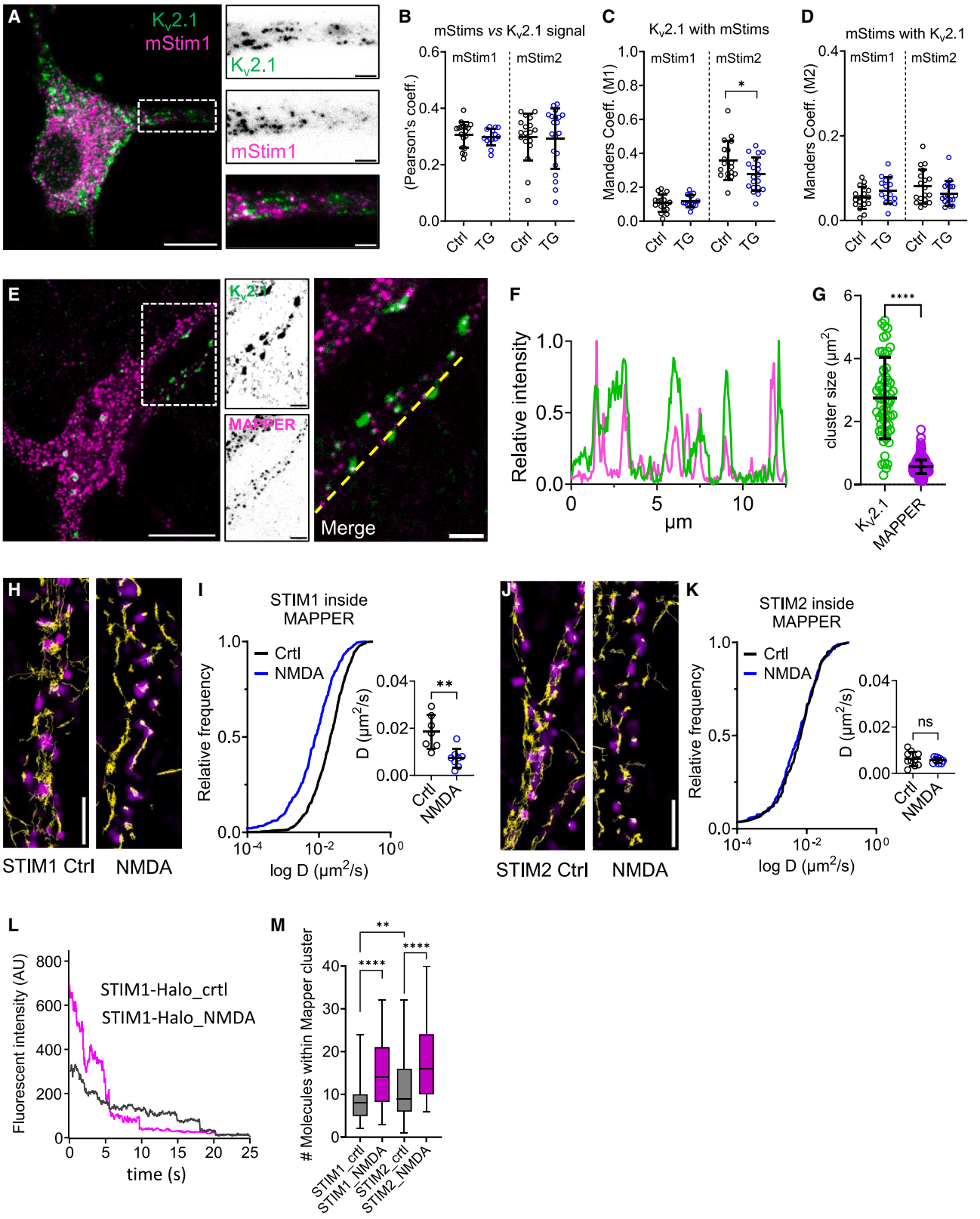

(legend on next page)

in MAPPER spots (Figures 6H–6K). SPT experiments confirmed that at rest, STIM1 exhibited equal diffusion inside and outside of MAPPER-positive regions (Figures 6J and 6K).

Bleaching of individually Halo-tagged STIMs allowed us to quantify the number of STIMs within MAPPER spots, leveraging the covalent 1:1 labeling stoichiometry between each Halo-tagged protein and its fluorescent ligand. The discrete photobleaching steps observed in fluorescence intensity traces of single STIM clusters (Figure 6L) enabled the direct counting of STIMs, consistent with previous reports.[60] In control conditions, there was a significant difference between the numbers of STIM1 and STIM2 within MAPPER spots (Figure 6M). Triggering STIM clustering by the activation of NMDARs increased the confinement of STIM1 inside the MAPPER spots but did not alter the diffusion properties of STIM2 therein (Figures 6I and 6K). Counting STIMs post-NMDA application showed a significant increase in trapped STIM1s and STIM2s within MAPPER-labelled ER-PM junctions (Figure 6M). This indicates that STIMs are recruited to ER-PM junctions during NMDAR activation. Although no obvious change in STIM2 mobility within MAPPER spots was detected, the number of STIM2s within these spots nearly doubled. This NMDA-induced relocation and confinement of STIMs within ER-PM junctions defined by MAPPER provides strong evidence for the diffusion trap model of STIM activation. Unlike STIM1, STIM2 was confined within MAPPER puncta under control conditions, which is even more evident in older cultures (DIV21–28). The observation confirms that STIM2 acts as a pre-positioned component. In contrast, STIM1 remained mobile at rest and relocated to MAPPER-positive ER-PM junctions after NMDA application, likely interacting within the pre-existing STIM2 clusters.[39,61] These experiments suggest that a fraction of ER-PM junctions occupied by STIM2s participates in the steady-state communication between the PM and the ER. The ER-PM junctions are dynamically populated by STIMs that are recruited upon the activation of NMDARs, whereas the junctions themselves are static (control: diff. coeff. MAPPER: 0.0017 $\mu m^2/s$, IQR: 0.0009/0.0015, NMDA activation: diff. coeff. MAPPER: 0.0013 $\mu m^2/s$ IQR: 0.0006/0.0023).

DISCUSSION

The precision of intracellular calcium signaling is essential for many neuronal functions, particularly within chemical synapses. Although STIMs are shown to be functionally important for synaptic communication between neurons,[20,46,47,62] the relationship between the position and function of proteins assigned to SOCE in neurons remains obscure. We employed SPT to examine the organization of STIMs within the ER membrane, as well as their localization and connections to the PM. SPT experiments provide the spatial and temporal resolution to explore the dynamic behavior of STIMs in the synaptic compartments. In non-excitable cells, STIMs are only transiently confined to spatially defined signaling compartments.[63–65] Using three distinct approaches in neurons to monitor endogenous, overexpressed, and re-expressed Halo-tagged STIMs, we demonstrate that STIMs are highly dynamic within the ER membrane and are transiently confined to ER-PM junctions. Differences in the sensitivity of STIMs to Ca^{2+} changes within the ER are reflected in the molecule numbers within clusters and dynamics of STIM1 and STIM2. Using a CRISPR-Cas9-based endogenous labeling strategy, we observed that dynamics are biased using specific splice variants or overexpression of STIMs (Figures 1H and S3). Differences in the mobility of overexpressed STIMs between DIV14 and DIV21–28 are explained by developmental changes in the ER architecture, as reported recently.[41] Modulating neuronal activity confirmed that STIM mobility is sensitive to neuronal excitability and network activity (Figures 4 and S4) and is altered by the tonic activity of NMDARs (Figure 4I). Strong activation of glutamatergic transmission directly links STIM mobility to fluctuations in ER calcium concentration. NMDAR activation serves as the predominant signal to trap STIMs within ER-PM junctions.[19,20] We did not find evidence that $Ca_V1.2$ channels are influenced by the confinement of STIMs, nor that these channels play a role in the clustering of STIMs.

ER-PM junctions containing STIMs may serve as structural elements to ensure that local calcium signals, triggered by the opening of NMDARs, are effectively relayed to ER effectors such as RyRs. We show that molecule numbers and cluster

Figure 6. Colocalization and dynamics of Kv2.1, STIM1, and STIM2 within ER-PM junctions

(A) Immunolabeling of Kv2.1 (green) and STIM1 (magenta) in hippocampal neurons.

(B–D) Quantification of colocalization between Kv2.1 and STIMs with Manders' overlap coefficients (M1 and M2), and Pearson's correlation coefficient before and after store depletion induced by 1 μM TG. (B) M1 represents the fraction of the STIMs signal that overlaps with the Kv2.1 signal. (C) M2 quantifies the fraction of the Kv2.1 signal that overlaps with the STIMs signal. (D) Pearson's correlation coefficient measuring the linear correlation between the STIM1 and Kv2.1 signals.

(E) Immunolabeling of Kv2.1 and MAPPER: representative images of hippocampal neurons immunolabeled for Kv2.1 (green) and MAPPER (magenta). MAPPER-GFP was overexpressed and delivered via rAAV. Scale bars, 20 μm for the full image and 2 μm for the enlarged section.

(F) Line plot analysis of Kv2.1 and MAPPER signal intensity across the dendritic region.

(G) Size of Kv2.1 and MAPPER clusters from two cultures (10 neurons each).

(H and J) (H) Example of Mapper clusters (magenta) and trajectories of STIM1 (yellow) along a dendritic segment for treatments as indicated, and (J) Similar for STIM2.

(I and K) Diffusion coefficients for STIMs within MAPPER spots under control conditions and after NMDA treatment. Median diffusion coefficient from one ROI encompassing multiple MAPPER spots.

(L) Photobleaching analysis of STIM clusters within MAPPER spots. Bleaching curves were used to estimate the number of STIM molecules per MAPPER cluster. Representative examples are shown, showing a single fluorophore bleaching step in the end.

(M) Quantification of STIM1s and STIM2s within MAPPER spots under control and NMDA-stimulated conditions. Error bars indicate the mean ± SD. Statistical significance is indicated as $^{****}p < 0.0001$, $^{***}p < 0.001$, and $^{*}p < 0.1$. For comparisons between two groups, a parametric unpaired *t* test was used, while multiple groups were analyzed using one-way ANOVA followed by Tukey's multiple comparisons test. Refer to supplemental table showing data for Figure 6 for details.

size change in response to NMDAR activation (Figures 4 and 6), supporting the idea that STIM-populated ER-PM junctions are structural elements connecting the ER with the PM. We assume that STIM-mediated ER-PM contacts link calcium signals between the PM and the ER, as studied in other cell types.[66,67] We found only a few STIM clusters within synapses, suggesting that peri-synaptic ER-PM junctions are sufficient to modulate the coupling of synaptic calcium signals to ER calcium stores. This hypothesis aligns with findings from functional studies.[46,47]

In HEK cells, clusters of STIM2 were shown to act as sites of pre-defined Ca^{2+} signaling hubs that recruit STIM1 upon stimulation.[66] Our data propose a similar mechanism in neurons. Using MAPPER as genetic marker of ER-PM junctions, we show that STIM2s are confined in ER-PM junctions already at rest. STIM1 is recruited to these clusters upon stronger ER Ca^{2+} store depletion (Figure 6). Interestingly, the number of STIMs in neuronal ER-PM junctions was almost identical to the number reported for HeLa cells.[60] The importance of SOCE for non-excitable cells[37] and the controversy regarding the physiological relevance of SOCE in neurons,[12] despite similar numbers of STIMs in ER-PM junctions, suggest SOCE-independent roles in neurons.[3,20,22,47,53,68–71] Although a number of synaptic phenotypes involving STIMs have been proposed,[20,36,46,47,72] direct evidence for ORAI proteins in boutons or spines remains sparse.[21,62] There are indications for the local replenishment of ER compartments by SOCE-mediated coupling within synaptic spines.[72] However, SPT data failed to reveal any enrichment of STIMs in pre- or post-synaptic regions (Figures 2E-2J, 3A–3C, and S3). STIMs avoid both the pre- and postsynaptic compartment, and ER Ca^{2+} depletion did not affect the mobility of STIMs within the synapse. This is consistent with an EM study, showing that the ER does not have direct contact with the active zone or spine head.[15] Although ER structures are present in around 40% of dendritic spines,[14] EM data do not confirm contacts to the PSD.[15] Our immunocytochemical experiments show that colocalizations between synaptic markers and endogenous STIMs are weak (Figures 2A–2D). Interestingly, we observed a lower STIM2 expression in inhibitory than in excitatory neurons (Figure S6), indicating different functions of STIMs in these classes of neurons.

STIM2 has been proposed to impact the trafficking of AMPAR subunits to extra-synaptic sites and contribute to plasticity-induced increase in synaptic AMPARs expression.[73] STIM1 and STIM2 were shown to regulate the activity of AMPAR and NMDAR subunits.[17,23,24,26] Our data support that NMDARs are important for STIM clustering, which was much more robust than ER Ca^{2+} store depletion alone (Figures 4M–4J and 4K).

One candidate that could regulate the differential aggregation of STIMs is the interaction with lipids of the PM. The C terminus of STIMs contains the polybasic domain, which is responsible for interaction with PM lipids.[64] Recent data suggest that the canonical STIM-ORAI activating region is capable of interacting with lipids.[74] Importantly, decreasing the levels of cholesterol in the PM impaired TG-induced clustering of STIM1.[75] Indeed, glutamate-induced clustering of STIM1Δk was less strong than that of wild-type STIM1 (Figure 4H). Other data suggest an interplay between the activity of NMDAR, lipids, and lipid transporters. Sun et al. (2019) showed that NMDAR stimulation causes the dissociation of TMEM24, a lipid transporter, from ER-PM junctions and that TMEM24 occupied the same population of ER-PM contacts as $K_V2.1$.[76] Clusters of both TMEM24 and $K_V2.1$ dissolved upon NMDAR stimulation, while in our experiments, the same treatment induced a massive clustering of STIMs (Figures 5 and S7). Ganglioside GM1 is reported to be associated with phosphorylated NMDARs in ER-PM junctions, and GM1 accumulation increased NMDAR currents, leading to spine enlargement.[77]

Glutamate-induced clustering of STIMs is driven by NMDARs, while AMPARs or $Ca_V1.2$ channels are not involved, despite the reported role of STIMs as inhibitors of $Ca_V1.2$ channels.[3,20,53,78,79] The work by Wang et al. (2010) investigated the effect of STIMs on the activity of $Ca_V1.2$ channels in HEK cells, reporting a significant decrease of $Ca_V1.2$ currents. Similar conclusions were reached by Park et al. (2010) and Dittmer et al. (2017), who showed that STIM1 inhibits $Ca_V1.2$ channels in neuronal cells. We utilized both HEK cells stably expressing $Ca_V1.2$ channels and mouse neuronal cultures. Our data do not support a direct effect of STIMs on the activity of $Ca_V1.2$ channels. The results agree with a study in cardiomyocytes reporting an increase in $Ca_V1.2$ currents upon STIM1 overexpression, which speaks against an inhibition.[80] Other data show that the overexpression of STIM1 had no impact on $Ca_V1.2$ currents, neither in physiological conditions nor when the currents were augmented by BayK.[81] Similar results were obtained by using a neuroblastoma cell line, where the overexpression of STIM1 had little impact on K^+-evoked Ca^{2+} influx into the cytosol.[36] Our data show that the knockdown of STIM1 or STIM2 in mouse hippocampal neurons did not augment depolarization-induced Ca^{2+} influx (Figures 5I and 5J). In HEK-cells, ER store depletion or STIM1 overexpression failed to attenuate whole-cell $Ca_V1.2$ currents (Figures 5N–5Q). Moreover, inhibition or activation of $Ca_V1.2$ by nim and BayK, respectively, did not change the dynamic behavior of STIMs or the degree of NMDA-induced ER Ca^{2+} depletion (Figures 5 and S4M). Altogether, our data do not confirm a function of STIMs as direct inhibitors of $Ca_V1.2$ channels nor did the $Ca_V1.2$-dependent Ca^{2+} influx impact STIM dynamics. In fact, $Ca_V1.2$ channels colocalize with $K_V2.1$ in ER-PM junctions,[55,56] while STIMs are only partially colocalized on the periphery with $K_V2.1$ clusters (Figures 6A–6D and S7).

Our SPT experiments reveal that STIMs are highly diffusive, and their mobility changes upon various stimuli that modulate neuronal activity. Whether clustered STIMs are functional units linked to ORAI channels in the PM is rather unlikely, since SOCE in neurons is very small compared to non-excitable cells.[12] NMDARs play a central role in the organization of STIMs, but $Ca_V1.2$ channels seem not to be involved. Neuronal STIMs are primarily localized in extra-synaptic regions in axons and dendrites. As a recent publication proposes,[19] the primary function of STIMs may be to regulate the spatial proximity between effector molecules in the PM and the ER membrane. A structural study on ER-PM contacts shows that regularly spaced ER-PM contacts are organized by junctophilins and STIMs to support long-range dendritic signal integration.[82] These contacts are absent from dendritic spines, confirming our data.

Communication between PM calcium entry and ER-mediated CICR does not always require perfect colocalization to be

functionally effective.[83] However, it is more efficient if the spatial distance between membranes is reduced. Therefore, we propose that STIM2 primarily maintains ER-PM contacts, while STIM1 enlarges these connections in an activity-dependent manner. This process is reversible even after prolonged NMDAR activation. The different affinities of STIM2 and STIM1 to changes in ER calcium content are well tuned to dynamically control the extent of ER-PM junctions. This does not exclude the possibility that prolonged clustering of STIMs could induce the accumulation of other proteins within ER-PM contacts. These proteins may not interact with STIMs but become trapped within the crowded environment of the ER-PM junction, comparable to other specialized membrane areas like pre- or postsynaptic membranes.[84]

Limitations of the study

The present work explored the dynamics of STIMs in cultured mouse hippocampal neurons, a widely used model to monitor neuronal function. Nevertheless, the physiological relevance of the observed phenotypes should be confirmed in *in vivo* studies. Similarly, the potential clinical impact of our observations in neuropathological conditions as epilepsy or stroke should be evaluated, e.g., with the use of different experimental systems. A differential role of STIMs depending on neuronal cell type is suggested by the lower expression of STIM2 in GABAergic neurons. Therefore, the exploration of cell-specific expression and modulation needs to be addressed in future studies.

To avoid the overexpression bias, we have confirmed the most crucial experiments with the use of CRISPR-mediated knockin constructs. The knockin and overexpression data are largely convergent, which confirms the relevance of our experimental approach. However, it cannot be excluded that the experiments that were not validated with the knockin approach could be biased by overexpression artifacts.

RESOURCE AVAILABILITY

Lead contact

Further information and requests for materials and data should be directed to and will be fulfilled by the lead contact, Martin Heine (marthein@uni-mainz.de).

Materials availability

This study did not generate any new materials.

Data and code availability

All data reported in this paper will be made available upon request by the lead contact. No code was generated in this study.

Any additional information required to reanalyze the data reported in this work paper is available from the lead contact upon request.

ACKNOWLEDGMENTS

We thank Anita Heine, Ana Carolina Amaral, Michela Borghi, Corinna Werkmann, and Abderazzaq El Khallouqi for preparing neuronal cultures, as well as Nathalie Philipp for their lab support. Further, we thank Jennifer Heck, Anna Bodzeta, and Junaid Akhtar for helping in initial experiments and fruitful discussions. We thank the imaging core facility of the JGU and Christoph Rickert for support in imaging and data analysis. We would like to thank Dr. Henning Draheim from Boehringer Ingelheim Pharma GmbH & Co. KG, Department CNS Diseases, for providing us with the stable HEK cell line expressing $Ca_V1.2$ channels. This work was supported by the DFG Germany research unit 2419 (Project P4) to M.H., the CRC1080 to M.H., and the Leibniz project SynERCa to M.H.

AUTHOR CONTRIBUTIONS

A.C. and M.H. performed SPT-SMLM microscopy. A.C. optimized and acquired SPT and performed WB, qRT-PCR, vector cloning, and rAAV design and production. F.M. conducted calcium imaging, confocal microscopy, and electrophysiological experiments. N.S. created STIM knockin constructs. N.S. and M.H. optimized the CRISPR-Cas protocol for knockins. A.C., F.M., and M.H. analyzed the data. M.H. provided funding and conceptualized the work, with input from A.C. and F.M. A.C., F.M., and M.H. wrote the manuscript.

DECLARATION OF INTERESTS

The authors declare that there are no competing interests associated with the manuscript.

STAR★METHODS

Detailed methods are provided in the online version of this paper and include the following:

- KEY RESOURCES TABLE
- EXPERIMENTAL MODEL AND STUDY PARTICIPANT DETAILS
  - Primary hippocampal neuronal cultures
  - HEK 293T cell culture
  - HEK 293 $Ca_V1.2$ cell culture for electrophysiology
- METHOD DETAILS
  - Transfection of cell line
  - Transduction of hippocampal neuronal cultures
  - Knockdown of STIMs
  - Generation of CRISPR-Cas9 STIM1/STIM2 knock-ins
  - Recombinant DNA
  - Antibodies and chemicals
  - HaloTag labeling
  - AAV production
  - Western Blotting
  - qRT PCR
  - Cytosolic Ca^{2+} imaging
  - ER Ca^{2+} imaging
  - Patch-clamp
  - Immunolabeling and confocal microscopy
- QUANTIFICATION AND STATISTICAL ANALYSIS
  - SPT acquisition and analysis
  - Workflow of SPT experiment
  - Analysis of cluster density and stoichiometry

SUPPLEMENTAL INFORMATION

Supplemental information can be found online at https://doi.org/10.1016/j.celrep.2025.116290.

Received: December 26, 2024
Revised: June 13, 2025
Accepted: August 25, 2025
Published: September 16, 2025

REFERENCES

1. Orci, L., Ravazzola, M., Le Coadic, M., Shen, W.W., Demaurex, N., and Cosson, P. (2009). From the Cover: STIM1-induced precortical and cortical subdomains of the endoplasmic reticulum. Proc. Natl. Acad. Sci. USA *106*, 19358–19362. https://doi.org/10.1073/pnas.0911280106.

2. Ambudkar, I.S., de Souza, L.B., and Ong, H.L. (2017). TRPC1, Orai1, and STIM1 in SOCE: Friends in tight spaces. Cell Calcium *63*, 33–39. https://doi.org/10.1016/j.ceca.2016.12.009.

3. Wang, Y., Deng, X., Mancarella, S., Hendron, E., Eguchi, S., Soboloff, J., Tang, X.D., and Gill, D.L. (2010). The calcium store sensor, STIM1, reciprocally controls Orai and CaV1.2 channels. Science *330*, 105–109. https://doi.org/10.1126/science.1191086.

4. Yuan, J.P., Zeng, W., Dorwart, M.R., Choi, Y.J., Worley, P.F., and Muallem, S. (2009). SOAR and the polybasic STIM1 domains gate and regulate Orai channels. Nat. Cell Biol. *11*, 337–343. https://doi.org/10.1038/ncb1842.

5. Putney, J.W., Jr., Broad, L.M., Braun, F.J., Lievremont, J.P., and Bird, G.S. (2001). Mechanisms of capacitative calcium entry. J. Cell Sci. *114*, 2223–2229. https://doi.org/10.1242/jcs.114.12.2223.

6. Voelkers, M., Salz, M., Herzog, N., Frank, D., Dolatabadi, N., Frey, N., Gude, N., Friedrich, O., Koch, W.J., Katus, H.A., et al. (2010). Orai1 and Stim1 regulate normal and hypertrophic growth in cardiomyocytes. J. Mol. Cell. Cardiol. *48*, 1329–1334. https://doi.org/10.1016/j.yjmcc.2010.01.020.

7. Gross, S.A., Wissenbach, U., Philipp, S.E., Freichel, M., Cavalié, A., and Flockerzi, V. (2007). Murine ORAI2 Splice Variants Form Functional Ca2+ Release-activated Ca2+ (CRAC) Channels. J. Biol. Chem. *282*, 19375–19384. https://doi.org/10.1074/jbc.M701962200.

8. Liou, J., Fivaz, M., Inoue, T., and Meyer, T. (2007). Live-cell imaging reveals sequential oligomerization and local plasma membrane targeting of stromal interaction molecule 1 after Ca2+ store depletion. Proc. Natl. Acad. Sci. USA *104*, 9301–9306. https://doi.org/10.1073/pnas.0702866104.

9. Roos, J., DiGregorio, P.J., Yeromin, A.V., Ohlsen, K., Lioudyno, M., Zhang, S., Safrina, O., Kozak, J.A., Wagner, S.L., Cahalan, M.D., et al. (2005). STIM1, an essential and conserved component of store-operated Ca2+ channel function. J. Cell Biol. *169*, 435–445. https://doi.org/10.1083/jcb.200502019.

10. Dziadek, M.A., and Johnstone, L.S. (2007). Biochemical properties and cellular localisation of STIM proteins. Cell Calcium *42*, 123–132. https://doi.org/10.1016/j.ceca.2007.02.006.

11. Klejman, M.E., Gruszczynska-Biegala, J., Skibinska-Kijek, A., Wisniewska, M.B., Misztal, K., Blazejczyk, M., Bojarski, L., and Kuznicki, J. (2009). Expression of STIM1 in brain and puncta-like co-localization of STIM1 and ORAI1 upon depletion of Ca(2+) store in neurons. Neurochem. Int. *54*, 49–55. https://doi.org/10.1016/j.neuint.2008.10.005.

12. Lu, B., and Fivaz, M. (2016). Neuronal SOCE: Myth or Reality? Trends Cell Biol. *26*, 890–893. https://doi.org/10.1016/j.tcb.2016.09.008.

13. Giordano, F., Saheki, Y., Idevall-Hagren, O., Colombo, S.F., Pirruccello, M., Milosevic, I., Gracheva, E.O., Bagriantsev, S.N., Borgese, N., and De Camilli, P. (2013). PI(4,5)P2-Dependent and Ca2+-Regulated ER-PM Interactions Mediated by the Extended Synaptotagmins. Cell *153*, 1494–1509. https://doi.org/10.1016/j.cell.2013.05.026.

14. Perez-Alvarez, A., Yin, S., Schulze, C., Hammer, J.A., Wagner, W., and Oertner, T.G. (2020). Endoplasmic reticulum visits highly active spines and prevents runaway potentiation of synapses. Nat. Commun. *11*, 5083. https://doi.org/10.1038/s41467-020-18889-5.

15. Wu, Y., Whiteus, C., Xu, C.S., Hayworth, K.J., Weinberg, R.J., Hess, H.F., and De Camilli, P. (2017). Contacts between the endoplasmic reticulum and other membranes in neurons. Proc. Natl. Acad. Sci. USA *114*, E4859–E4867. https://doi.org/10.1073/pnas.1701078114.

16. Lalonde, J., Saia, G., and Gill, G. (2014). Store-operated calcium entry promotes the degradation of the transcription factor Sp4 in resting neurons. Sci. Signal. *7*, ra51. https://doi.org/10.1126/scisignal.2005242.

17. Serwach, K., and Gruszczynska-Biegala, J. (2020). Target Molecules of STIM Proteins in the Central Nervous System. Front. Mol. Neurosci. *13*, 617422. https://doi.org/10.3389/fnmol.2020.617422.

18. Emptage, N.J., Reid, C.A., and Fine, A. (2001). Calcium Stores in Hippocampal Synaptic Boutons Mediate Short-Term Plasticity, Store-Operated Ca2+ Entry, and Spontaneous Transmitter Release. Neuron *29*, 197–208. https://doi.org/10.1016/S0896-6273(01)00190-8.

19. Dittmer, P.J., and Dell'Acqua, M.L. (2024). L-type Ca(2+) channel activation of STIM1-Orai1 signaling remodels the dendritic spine ER to maintain long-term structural plasticity. Proc. Natl. Acad. Sci. USA *121*, e2407324121. https://doi.org/10.1073/pnas.2407324121.

20. Dittmer, P.J., Wild, A.R., Dell'Acqua, M.L., and Sather, W.A. (2017). STIM1 Ca(2+) Sensor Control of L-type Ca(2+)-Channel-Dependent Dendritic Spine Structural Plasticity and Nuclear Signaling. Cell Rep. *19*, 321–334. https://doi.org/10.1016/j.celrep.2017.03.056.

21. Basnayake, K., Mazaud, D., Kushnireva, L., Bemelmans, A., Rouach, N., Korkotian, E., and Holcman, D. (2021). Nanoscale molecular architecture controls calcium diffusion and ER replenishment in dendritic spines. Sci. Adv. *7*, eabh1376. https://doi.org/10.1126/sciadv.abh1376.

22. Garcia-Alvarez, G., Shetty, M.S., Lu, B., Yap, K.A.F., Oh-Hora, M., Sajikumar, S., Bichler, Z., and Fivaz, M. (2015). Impaired spatial memory and enhanced long-term potentiation in mice with forebrain-specific ablation of the Stim genes. Front. Behav. Neurosci. *9*, 180. https://doi.org/10.3389/fnbeh.2015.00180.

23. Gruszczynska-Biegala, J., Sladowska, M., and Kuznicki, J. (2016). AMPA Receptors Are Involved in Store-Operated Calcium Entry and Interact with STIM Proteins in Rat Primary Cortical Neurons. Front. Cell. Neurosci. *10*, 251. https://doi.org/10.3389/fncel.2016.00251.

24. Gruszczynska-Biegala, J., Strucinska, K., Maciag, F., Majewski, L., Sladowska, M., and Kuznicki, J. (2020). STIM Protein-NMDA2 Receptor Interaction Decreases NMDA-Dependent Calcium Levels in Cortical Neurons. Cells *9*, 160. https://doi.org/10.3390/cells9010160.

25. Maneshi, M.M., Toth, A.B., Ishii, T., Hori, K., Tsujikawa, S., Shum, A.K., Shrestha, N., Yamashita, M., Miller, R.J., Radulovic, J., et al. (2020). Orai1 Channels Are Essential for Amplification of Glutamate-Evoked Ca(2+) Signals in Dendritic Spines to Regulate Working and Associative Memory. Cell Rep. *33*, 108464. https://doi.org/10.1016/j.celrep.2020.108464.

26. Serwach, K., Nurowska, E., Klukowska, M., Zablocka, B., and Gruszczynska-Biegala, J. (2023). STIM2 regulates NMDA receptor endocytosis that is induced by short-term NMDA receptor overactivation in cortical neurons. Cell. Mol. Life Sci. *80*, 368. https://doi.org/10.1007/s00018-023-05028-8.

27. Yap, K.A.F., Shetty, M.S., Garcia-Alvarez, G., Lu, B., Alagappan, D., Oh-Hora, M., Sajikumar, S., and Fivaz, M. (2017). STIM2 regulates AMPA receptor trafficking and plasticity at hippocampal synapses. Neurobiol. Learn. Mem. *138*, 54–61. https://doi.org/10.1016/j.nlm.2016.08.007.

28. Maciag, F., Chhikara, A., and Heine, M. (2024). Calcium channel signalling at neuronal endoplasmic reticulum-plasma membrane junctions. Biochem. Soc. Trans. *52*, 1617–1629. https://doi.org/10.1042/BST20230819.

29. Gil, D., Guse, A.H., and Dupont, G. (2021). Three-Dimensional Model of Sub-Plasmalemmal Ca2+ Microdomains Evoked by the Interplay Between ORAI1 and InsP3 Receptors. Front. Immunol. *12*, 659790. https://doi.org/10.3389/fimmu.2021.659790.

30. Prakriya, M., and Lewis, R.S. (2015). Store-Operated Calcium Channels. Physiol. Rev. *95*, 1383–1436. https://doi.org/10.1152/physrev.00020.2014.

31. Wu, M.M., Covington, E.D., and Lewis, R.S. (2014). Single-molecule analysis of diffusion and trapping of STIM1 and Orai1 at endoplasmic reticulum-plasma membrane junctions. Mol. Biol. Cell *25*, 3672–3685. https://doi.org/10.1091/mbc.E14-06-1107.

32. Ryazantseva, M., Goncharova, A., Skobeleva, K., Erokhin, M., Methner, A., Georgiev, P., and Kaznacheyeva, E. (2018). Presenilin-1 Delta E9 Mutant Induces STIM1-Driven Store-Operated Calcium Channel Hyperactivation in Hippocampal Neurons. Mol. Neurobiol. *55*, 4667–4680. https://doi.org/10.1007/s12035-017-0674-4.

33. Skibinska-Kijek, A., Wisniewska, M.B., Gruszczynska-Biegala, J., Methner, A., and Kuznicki, J. (2009). Immunolocalization of STIM1 in the mouse brain. Acta Neurobiol. Exp. *69*, 413–428. https://doi.org/10.55782/ane-2009-1753.

34. Zhang, M., Song, J.N., Wu, Y., Zhao, Y.L., Pang, H.G., Fu, Z.F., Zhang, B.F., and Ma, X.D. (2014). Suppression of STIM1 in the early stage after global ischemia attenuates the injury of delayed neuronal death by

inhibiting store-operated calcium entry-induced apoptosis in rats. Neuroreport *25*, 507–513. https://doi.org/10.1097/wnr.0000000000000127.

35. Miederer, A.M., Alansary, D., Schwär, G., Lee, P.H., Jung, M., Helms, V., and Niemeyer, B.A. (2015). A STIM2 splice variant negatively regulates store-operated calcium entry. Nat. Commun. *6*, 6899. https://doi.org/10.1038/ncomms7899.

36. Ramesh, G., Jarzembowski, L., Schwarz, Y., Poth, V., Konrad, M., Knapp, M.L., Schwär, G., Lauer, A.A., Grimm, M.O.W., Alansary, D., et al. (2021). A short isoform of STIM1 confers frequency-dependent synaptic enhancement. Cell Rep. *34*, 108844. https://doi.org/10.1016/j.celrep.2021.108844.

37. Rosado, J.A., Diez, R., Smani, T., and Jardín, I. (2015). STIM and Orai1 Variants in Store-Operated Calcium Entry. Front. Pharmacol. *6*, 325. https://doi.org/10.3389/fphar.2015.00325.

38. Gruszczynska-Biegala, J., Pomorski, P., Wisniewska, M.B., and Kuznicki, J. (2011). Differential roles for STIM1 and STIM2 in store-operated calcium entry in rat neurons. PLoS One *6*, e19285. https://doi.org/10.1371/journal.pone.0019285.

39. Ong, H.L., de Souza, L.B., Zheng, C., Cheng, K.T., Liu, X., Goldsmith, C. M., Feske, S., and Ambudkar, I.S. (2015). STIM2 enhances receptor-stimulated Ca^{2+} signaling by promoting recruitment of STIM1 to the endoplasmic reticulum-plasma membrane junctions. Sci. Signal. *8*, ra3. https://doi.org/10.1126/scisignal.2005748.

40. Domanov, Y.A., Aimon, S., Toombes, G.E.S., Renner, M., Quemeneur, F., Triller, A., Turner, M.S., and Bassereau, P. (2011). Mobility in geometrically confined membranes. Proc. Natl. Acad. Sci. USA *108*, 12605–12610. https://doi.org/10.1073/pnas.1102646108.

41. Zamponi, E., Meehl, J.B., and Voeltz, G.K. (2022). The ER ladder is a unique morphological feature of developing mammalian axons. Dev. Cell *57*, 1369–1382.e6. https://doi.org/10.1016/j.devcel.2022.05.002.

42. Klatt, O., Repetto, D., Brockhaus, J., Reissner, C., El Khallouqi, A., Rohlmann, A., Heine, M., and Missler, M. (2021). Endogenous beta-neurexins on axons and within synapses show regulated dynamic behavior. Cell Rep. *35*, 109266. https://doi.org/10.1016/j.celrep.2021.109266.

43. Lee, Y., Park, S., Yuan, F., Hayden, C.C., Wang, L., Lafer, E.M., Choi, S.Q., and Stachowiak, J.C. (2023). Transmembrane coupling of liquid-like protein condensates. Nat. Commun. *14*, 8015. https://doi.org/10.1038/s41467-023-43332-w.

44. Oh-Hora, M., Yamashita, M., Hogan, P.G., Sharma, S., Lamperti, E., Chung, W., Prakriya, M., Feske, S., and Rao, A. (2008). Dual functions for the endoplasmic reticulum calcium sensors STIM1 and STIM2 in T cell activation and tolerance. Nat. Immunol. *9*, 432–443. https://doi.org/10.1038/ni1574.

45. Willems, J., de Jong, A.P.H., Scheefhals, N., Mertens, E., Catsburg, L.A.E., Poorthuis, R.B., de Winter, F., Verhaagen, J., Meye, F.J., and MacGillavry, H.D. (2020). ORANGE: A CRISPR/Cas9-based genome editing toolbox for epitope tagging of endogenous proteins in neurons. PLoS Biol. *18*, e3000665. https://doi.org/10.1371/journal.pbio.3000665.

46. Chanaday, N.L., Nosyreva, E., Shin, O.H., Zhang, H., Aklan, I., Atasoy, D., Bezprozvanny, I., and Kavalali, E.T. (2021). Presynaptic store-operated Ca(2+) entry drives excitatory spontaneous neurotransmission and augments endoplasmic reticulum stress. Neuron *109*, 1314–1332.e5. https://doi.org/10.1016/j.neuron.2021.02.023.

47. de Juan-Sanz, J., Holt, G.T., Schreiter, E.R., de Juan, F., Kim, D.S., and Ryan, T.A. (2017). Axonal Endoplasmic Reticulum Ca2+ Content Controls Release Probability in CNS Nerve Terminals. Neuron *93*, 867–881.e866. https://doi.org/10.1016/j.neuron.2017.01.010.

48. Kushnireva, L., Korkotian, E., and Segal, M. (2020). Calcium Sensors STIM1 and STIM2 Regulate Different Calcium Functions in Cultured Hippocampal Neurons. Front. Synaptic Neurosci. *12*, 573714. https://doi.org/10.3389/fnsyn.2020.573714.

49. Chanaday, N.L., and Kavalali, E.T. (2022). Role of the endoplasmic reticulum in synaptic transmission. Curr. Opin. Neurobiol. *73*, 102538. https://doi.org/10.1016/j.conb.2022.102538.

50. Maggio, N., and Vlachos, A. (2014). Synaptic plasticity at the interface of health and disease: New insights on the role of endoplasmic reticulum intracellular calcium stores. Neuroscience *281*, 135–146. https://doi.org/10.1016/j.neuroscience.2014.09.041.

51. Ng, A.N., Krogh, M., and Toresson, H. (2011). Dendritic EGFP-STIM1 activation after type I metabotropic glutamate and muscarinic acetylcholine receptor stimulation in hippocampal neuron. J. Neurosci. Res. *89*, 1235–1244. https://doi.org/10.1002/jnr.22648.

52. Zhou, Y., Srinivasan, P., Razavi, S., Seymour, S., Meraner, P., Gudlur, A., Stathopulos, P.B., Ikura, M., Rao, A., and Hogan, P.G. (2013). Initial activation of STIM1, the regulator of store-operated calcium entry. Nat. Struct. Mol. Biol. *20*, 973–981. https://doi.org/10.1038/nsmb.2625.

53. Park, C.Y., Shcheglovitov, A., and Dolmetsch, R. (2010). The CRAC channel activator STIM1 binds and inhibits L-type voltage-gated calcium channels. Science *330*, 101–105. https://doi.org/10.1126/science.1191027.

54. Mandikian, D., Bocksteins, E., Parajuli, L.K., Bishop, H.I., Cerda, O., Shigemoto, R., and Trimmer, J.S. (2014). Cell type-specific spatial and functional coupling between mammalian brain Kv2.1 K+ channels and ryanodine receptors. J. Comp. Neurol. *522*, 3555–3574. https://doi.org/10.1002/cne.23641.

55. Vierra, N.C., Kirmiz, M., van der List, D., Santana, L.F., and Trimmer, J.S. (2019). Kv2.1 mediates spatial and functional coupling of L-type calcium channels and ryanodine receptors in mammalian neurons. eLife *8*, e49953. https://doi.org/10.7554/eLife.49953.

56. Vierra, N.C., O'Dwyer, S.C., Matsumoto, C., Santana, L.F., and Trimmer, J. S. (2021). Regulation of neuronal excitation-transcription coupling by Kv2.1-induced clustering of somatic L-type Ca(2+) channels at ER-PM junctions. Proc. Natl. Acad. Sci. USA *118*, e2110094118. https://doi.org/10.1073/pnas.2110094118.

57. Johnson, B., Leek, A.N., and Tamkun, M.M. (2019). Kv2 channels create endoplasmic reticulum/plasma membrane junctions: a brief history of Kv2 channel subcellular localization. Channels *13*, 88–101. https://doi.org/10.1080/19336950.2019.1568824.

58. Misonou, H., Mohapatra, D.P., Park, E.W., Leung, V., Zhen, D., Misonou, K., Anderson, A.E., and Trimmer, J.S. (2004). Regulation of ion channel localization and phosphorylation by neuronal activity. Nat. Neurosci. *7*, 711–718.

59. Chang, C.-L., Hsieh, T.-S., Yang, T.T., Rothberg, K.G., Azizoglu, D.B., Volk, E., Liao, J.-C., and Liou, J. (2013). Feedback Regulation of Receptor-Induced Ca2+ Signaling Mediated by E-Syt1 and Nir2 at Endoplasmic Reticulum-Plasma Membrane Junctions. Cell Rep. *5*, 813–825. https://doi.org/10.1016/j.celrep.2013.09.038.

60. Shen, Y., Thillaiappan, N.B., and Taylor, C.W. (2021). The store-operated Ca(2+) entry complex comprises a small cluster of STIM1 associated with one Orai1 channel. Proc. Natl. Acad. Sci. USA *118*, e2010789118. https://doi.org/10.1073/pnas.2010789118.

61. Ahmad, M., Ong, H.L., Saadi, H., Son, G.-Y., Shokatian, Z., Terry, L.E., Trebak, M., Yule, D.I., and Ambudkar, I. (2022). Functional communication between IP_3R and STIM2 at subthreshold stimuli is a critical checkpoint for initiation of SOCE. Proc. Natl. Acad. Sci. USA *119*, e2114928118. https://doi.org/10.1073/pnas.2114928118.

62. Korkotian, E., Oni-Biton, E., and Segal, M. (2017). The role of the store-operated calcium entry channel Orai1 in cultured rat hippocampal synapse formation and plasticity. J. Physiol. *595*, 125–140. https://doi.org/10.1113/jp272645.

63. Deng, X., Wang, Y., Zhou, Y., Soboloff, J., and Gill, D.L. (2009). STIM and Orai: Dynamic Intermembrane Coupling to Control Cellular Calcium Signals. J. Biol. Chem. *284*, 22501–22505. https://doi.org/10.1074/jbc.R109.018655.

64. Sallinger, M., Grabmayr, H., Humer, C., Bonhenry, D., Romanin, C., Schindl, R., and Derler, I. (2024). Activation mechanisms and structural dynamics of STIM proteins. J. Physiol. *602*, 1475–1507. https://doi.org/10.1113/jp283828.

65. Soboloff, J., Rothberg, B.S., Madesh, M., and Gill, D.L. (2012). STIM proteins: dynamic calcium signal transducers. Nat. Rev. Mol. Cell Biol. *13*, 549–565. https://doi.org/10.1038/nrm3414.

66. Ahmad, M., Narayanasamy, S., Ong, H.L., and Ambudkar, I. (2022). STIM Proteins and Regulation of SOCE in ER-PM Junctions. Biomolecules *12*, 1152.

67. Carrasco, S., and Meyer, T. (2011). STIM proteins and the endoplasmic reticulum-plasma membrane junctions. Annu. Rev. Biochem. *80*, 973–1000. https://doi.org/10.1146/annurev-biochem-061609-165311.

68. Berna-Erro, A., Braun, A., Kraft, R., Kleinschnitz, C., Schuhmann, M.K., Stegner, D., Wultsch, T., Eilers, J., Meuth, S.G., Stoll, G., and Nieswandt, B. (2009). STIM2 regulates capacitive Ca2+ entry in neurons and plays a key role in hypoxic neuronal cell death. Sci. Signal. *2*, ra67. https://doi.org/10.1126/scisignal.2000522.

69. Lefkimmiatis, K., Srikanthan, M., Maiellaro, I., Moyer, M.P., Curci, S., and Hofer, A.M. (2009). Store-operated cyclic AMP signalling mediated by STIM1. Nat. Cell Biol. *11*, 433–442. https://doi.org/10.1038/ncb1850.

70. Majewski, Ł., Maciąg, F., Boguszewski, P.M., Wasilewska, I., Wiera, G., Wójtowicz, T., Mozrzymas, J., and Kuznicki, J. (2017). Overexpression of STIM1 in neurons in mouse brain improves contextual learning and impairs long-term depression. Biochim. Biophys. Acta. Mol. Cell Res. *1864*, 1071–1087. https://doi.org/10.1016/j.bbamcr.2016.11.025.

71. Tian, G., Tepikin, A.V., Tengholm, A., and Gylfe, E. (2012). cAMP induces stromal interaction molecule 1 (STIM1) puncta but neither Orai1 protein clustering nor store-operated Ca2+ entry (SOCE) in islet cells. J. Biol. Chem. *287*, 9862–9872. https://doi.org/10.1074/jbc.M111.292854.

72. Sun, S., Zhang, H., Liu, J., Popugaeva, E., Xu, N.J., Feske, S., White, C.L., 3rd, and Bezprozvanny, I. (2014). Reduced synaptic STIM2 expression and impaired store-operated calcium entry cause destabilization of mature spines in mutant presenilin mice. Neuron *82*, 79–93. https://doi.org/10.1016/j.neuron.2014.02.019.

73. Garcia-Alvarez, G., Lu, B., Yap, K.A.F., Wong, L.C., Thevathasan, J.V., Lim, L., Ji, F., Tan, K.W., Mancuso, J.J., Tang, W., et al. (2015). STIM2 regulates PKA-dependent phosphorylation and trafficking of AMPARs. Mol. Biol. Cell *26*, 1141–1159. https://doi.org/10.1091/mbc.E14-07-1222.

74. Cohen, H.A., Zomot, E., Nataniel, T., Militsin, R., and Palty, R. (2023). The SOAR of STIM1 interacts with plasma membrane lipids to form ER-PM contact sites. Cell Rep. *42*, 112238. https://doi.org/10.1016/j.celrep.2023.112238.

75. Pani, B., Ong, H.L., Liu, X., Rauser, K., Ambudkar, I.S., and Singh, B.B. (2008). Lipid rafts determine clustering of STIM1 in endoplasmic reticulum-plasma membrane junctions and regulation of store-operated Ca2+ entry (SOCE). J. Biol. Chem. *283*, 17333–17340. https://doi.org/10.1074/jbc.M800107200.

76. Sun, E.W., Guillén-Samander, A., Bian, X., Wu, Y., Cai, Y., Messa, M., and De Camilli, P. (2019). Lipid transporter TMEM24/C2CD2L is a Ca(2+)-regulated component of ER-plasma membrane contacts in mammalian neurons. Proc. Natl. Acad. Sci. USA *116*, 5775–5784. https://doi.org/10.1073/pnas.1820156116.

77. Weesner, J.A., Annunziata, I., van de Vlekkert, D., Robinson, C.G., Campos, Y., Mishra, A., Fremuth, L.E., Gomero, E., Hu, H., and d'Azzo, A. (2024). Altered GM1 catabolism affects NMDAR-mediated Ca(2+) signaling at ER-PM junctions and increases synaptic spine formation in a GM1-gangliosidosis model. Cell Rep. *43*, 114117. https://doi.org/10.1016/j.celrep.2024.114117.

78. Pascual-Caro, C., Espinosa-Bermejo, N., Pozo-Guisado, E., and Martin-Romero, F.J. (2018). Role of STIM1 in neurodegeneration. World J. Biol. Chem. *9*, 16–24. https://doi.org/10.4331/wjbc.v9.i2.16.

79. Sun, Y., Zhang, H., Selvaraj, S., Sukumaran, P., Lei, S., Birnbaumer, L., and Singh, B.B. (2017). Inhibition of L-Type Ca(2+) Channels by TRPC1-STIM1 Complex Is Essential for the Protection of Dopaminergic Neurons. J. Neurosci. *37*, 3364–3377. https://doi.org/10.1523/jneurosci.3010-16.2017.

80. Correll, R.N., Goonasekera, S.A., van Berlo, J.H., Burr, A.R., Accornero, F., Zhang, H., Makarewich, C.A., York, A.J., Sargent, M.A., Chen, X., et al. (2015). STIM1 elevation in the heart results in aberrant Ca2+ handling and cardiomyopathy. J. Mol. Cell. Cardiol. *87*, 38–47. https://doi.org/10.1016/j.yjmcc.2015.07.032.

81. Troupes, C.D., Wallner, M., Borghetti, G., Zhang, C., Mohsin, S., von Lewinski, D., Berretta, R.M., Kubo, H., Chen, X., Soboloff, J., and Houser, S. (2017). Role of STIM1 (Stromal Interaction Molecule 1) in Hypertrophy-Related Contractile Dysfunction. Circ. Res. *121*, 125–136. https://doi.org/10.1161/circresaha.117.311094.

82. Benedetti, L., Fan, R., Weigel, A.V., Moore, A.S., Houlihan, P.R., Kittisopikul, M., Park, G., Petruncio, A., Hubbard, P.M., Pang, S., et al. (2025). Periodic ER-plasma membrane junctions support long-range Ca(2+) signal integration in dendrites. Cell *188*, 484–500.e22. https://doi.org/10.1016/j.cell.2024.11.029.

83. Basnayake, K., Mazaud, D., Bemelmans, A., Rouach, N., Korkotian, E., and Holcman, D. (2019). Fast calcium transients in dendritic spines driven by extreme statistics. PLoS Biol. *17*, e2006202. https://doi.org/10.1371/journal.pbio.2006202.

84. Choquet, D., and Triller, A. (2013). The dynamic synapse. Neuron *80*, 691–703. https://doi.org/10.1016/j.neuron.2013.10.013.

85. Ortner, N.J., Bock, G., Dougalis, A., Kharitonova, M., Duda, J., Hess, S., Tuluc, P., Pomberger, T., Stefanova, N., Pitterl, F., et al. (2017). Lower Affinity of Isradipine for L-Type Ca(2+) Channels during Substantia Nigra Dopamine Neuron-Like Activity: Implications for Neuroprotection in Parkinson's Disease. J Neurosci *37*, 6761–6777. https://doi.org/10.1523/jneurosci.2946-16.2017.

86. Tamamaki, N., Yanagawa, Y., Tomioka, R., Miyazaki, J.I., Obata, K., and Kaneko, T. (2003). Green fluorescent protein expression and colocalization with calretinin, parvalbumin, and somatostatin in the GAD67-GFP knock-in mouse. J. Comp. Neurol. *467*, 60–79. https://doi.org/10.1002/cne.10905.

87. Prakriya, M., Feske, S., Gwack, Y., Srikanth, S., Rao, A., and Hogan, P.G. (2006). Orai1 is an essential pore subunit of the CRAC channel. Nature *443*, 230–233. https://doi.org/10.1038/nature05122.

88. Brandman, O., Liou, J., Park, W.S., and Meyer, T. (2007). STIM2 is a feedback regulator that stabilizes basal cytosolic and endoplasmic reticulum Ca2+ levels. Cell *131*, 1327–1339. https://doi.org/10.1016/j.cell.2007.11.039.

89. Koerber, J.T., Jang, J.H., Yu, J.H., Kane, R.S., and Schaffer, D.V. (2007). Engineering adeno-associated virus for one-step purification via immobilized metal affinity chromatography. Hum. Gene Ther. *18*, 367–378. https://doi.org/10.1089/hum.2006.139.

90. Kaspar, B.K., Vissel, B., Bengoechea, T., Crone, S., Randolph-Moore, L., Muller, R., Brandon, E.P., Schaffer, D., Verma, I.M., Lee, K.F., et al. (2002). Adeno-associated virus effectively mediates conditional gene modification in the brain. Proc. Natl. Acad. Sci. USA *99*, 2320–2325. https://doi.org/10.1073/pnas.042678699.

91. Xiong, W., MacColl Garfinkel, A.E., Li, Y., Benowitz, L.I., and Cepko, C.L. (2015). NRF2 promotes neuronal survival in neurodegeneration and acute nerve damage. J. Clin. Investig. *125*, 1433–1445. https://doi.org/10.1172/jci79735.

92. Butler, C., Saraceno, G.E., Kechkar, A., Bénac, N., Studer, V., Dupuis, J. P., Groc, L., Galland, R., and Sibarita, J.B. (2022). Multi-Dimensional Spectral Single Molecule Localization Microscopy. Front. Bioinform. *2*, 813494. https://doi.org/10.3389/fbinf.2022.813494.

93. Hummert, J., Yserentant, K., Fink, T., Euchner, J., Ho, Y.X., Tashev, S.A., and Herten, D.P. (2021). Photobleaching step analysis for robust determination of protein complex stoichiometries. Mol. Biol. Cell *32*, ar35. https://doi.org/10.1091/mbc.E20-09-0568.

STAR★METHODS

KEY RESOURCES TABLE

REAGENT or RESOURCE	SOURCE	IDENTIFIER
Antibodies		
Rabbit anti-STIM1 (N-terminal)	Sigma-Aldrich	Cat# S6072; RRID: AB_1079008
Rabbit anti-STIM2	Alomone Labs	Cat# ACC-064; RRID: AB_2040218
Mouse monoclonal anti-Beta-actin	Synaptic Systems	Cat# 251011; RRID: AB_2619960
Guinea pig polyclonal anti-Bassoon	Synaptic Systems	Cat# 141004; RRID: AB_2290619
Mouse monoclonal anti-Homer1	Synaptic Systems	Cat# 160011; RRID: AB_2120992
Mouse anti-RIM	Synaptic Systems	Cat# 140203; RRID: AB_887775
Mouse monoclonal anti-Ankyrin-G	Neuromab	Clone N106/36; RRID:AB_2877524
Mouse monoclonal anti-KV2.1	NeuroMab	Cat# 75-159; RRID: AB_2131649
Mouse monoclonal anti-MAP2	Synaptic Systems	Cat# 188011; RRID: AB_2147096
Rabbit polyclonal anti-NR2B	Alomone Labs	Cat# AGC-003; AB_2040028
HRP anti-Guinea Pig	Jackson ImmunoResearch	Cat# 706-035-148; RRID:AB_2340447
HRP anti-Mouse	Jackson ImmunoResearch	Cat# 115-035-146; RRID:AB_2307392
HRP anti-Rabbit	Jackson ImmunoResearch	Cat# 711-035-152; RRID:AB_10015282
Bacterial and virus strains		
rAAV-DJ-6xHis (Viral Coat)	This paper	Modified from Koerber et al., 2007
rAAV-DJ-6xHis: hSyn:Cre-P2A-TdTomato	This paper/Addgene	Addgene #107738
rAAV-DJ-6xHis: hSyn:ΔCre-P2A-TdTomato	This paper	N/A
rAAV-DJ-6xHis: hSyn:Halo-STIM1 (23–685aa)	This paper	N/A
rAAV-DJ-6xHis: hSyn:Halo-STIM2	This paper	N/A
rAAV-DJ-6xHis: hSyn:Halo-STIM1-deltaK	This paper	N/A
rAAV-DJ-6xHis: hSyn:Halo-TMC	This paper	N/A
rAAV-DJ-6xHis: hSyn:synaptophysin-GCaMP6f	This paper	N/A
rAAV-DJ-6xHis: hSyn:PSD-fingr-GFP	This paper	N/A
rAAV-DJ-6xHis/rAAV2: CMV::ER-GCaMP150	This paper	N/A
rAAV-DJ-6xHis/rAAV2: CMV::GFP-Mapper	This paper	N/A
rAAV-DJ-6xHis/rAAV2: CMV::GFP	This paper	N/A
rAAV-DJ-6xHis/rAAV2: GFP/Cre	This paper	N/A
Chemicals, peptides, and recombinant proteins		
DMEM	Gibco	Cat# 41966-029
Neurobasal Medium	Gibco	Cat# 12348-017
B27 Supplement	Gibco	Cat# 17504044
L-Glutamine	Gibco	Cat# 25030-024
Fetal Bovine Serum (FBS)	Thermo	Cat# V30160.03
HBSS	Sigma	Cat# H9394
Trypsin-EDTA (1×)	Gibco	Cat# 15400-054
Opti-MEM	Gibco	Cat# 31985-070
Poly-L-lysine/Poly-D-lysine	Sigma-Aldrich	Cat# P1149
Mowiol Mounting Medium	Roth	Cat# 713.2
Albumin Fraction V	Roth	CAS# 9048-46-8
Methanol	Roth	Cat# 7342.1
PVDF membrane	Roth	Cat# T830.1
Pierce ECL Western Substrate	Life Technologies	Cat# 32209

(*Continued on next page*)

Continued

REAGENT or RESOURCE	SOURCE	IDENTIFIER
PEI (Polyethylenimine)	Sigma-Aldrich	Cat# 408727
DHPG	HelloBio	Cat# HB0045
Bicuculline Methiodide	Tocris	Cat# 2503
Caffeine	Sigma-Aldrich	Cat# C0750
CNQX Disodium Salt	HelloBio/Tocris	HB0204/1045
Cyclopiazonic Acid (CPA)	HelloBio	Cat# HB1117
D-AP5/D-APV	HelloBio/Tocris	HB0225/0106
Ifenprodil	HelloBio	Cat# HB0339
L-Glutamate	Abcam	Cat# ab120049
MK 801 Maleate	HelloBio	Cat# HB0004
Nimodipine	Tocris	Cat# 0600/100
NMDA	HelloBio	Cat# HB0454
Ryanodine	HelloBio	Cat# HB1320
Thapsigargin (TG)	HelloBio	Cat# HB1118
Bay K 8644	Tocris	Cat# 1544
Critical commercial assays		
Halo-Tag 646	Promega	Cat# G9281
Fura-2 a.m.	Abcam	Cat# ab120873
SYBR Green dye	Life Technologies	Cat# 4367659
Trizol reagent	Thermo Fisher	Cat# 10296010
SuperScript III Reverse Transcriptase	Invitrogen	Cat# 18080051
RNAse Inhibitor	NEB	Cat# M0314L
DNAse I, RNase-free	Thermo Fisher	Cat# EN0521
RNeasy Mini spin column	Qiagen	Cat# 79523
Experimental models: Cell lines		
HEK 293T (293tsA1609*neo*)	DSMZ	ACC 635
HEK293T-CaV1.2 + auxiliary subunits	Boehringer Ingelheim	Ortner et al.[85]
Experimental models: Organisms/strains		
Mouse: Stim1$^{fl/fl}$, Strain: B6.Cg-Stim1^{tm1Rao}/J	Jackson Laboratory	JAX: 023350
Mouse: Stim2$^{fl/fl}$, Strain: B6.Cg-Stim2^{tm1Rao}/J	Jackson Laboratory	JAX: 023351
Mouse: GAD67-GFP knock-in	Tamamaki et al.[86]	N/A
Mouse: Rosa26-Cas9 knock-in, Gt(ROSA) 26Sor$^{tm1.1(CAG-cas9*,-EGFP)Fezh}$/J	Jackson Laboratory	IMSR_JAX:024858
Oligonucleotides		
Guide RNA (STIM1): 5′GTATTCTTTTCACTGTGACT	This paper	N/A
Guide RNA (STIM2): 5′CCCGCGGAGGTGCCGGGGCA	This paper	N/A
STIM1_F_2: 5′CCCTTGTCCATGCAGTATG	qRT-PCR: This paper	N/A
STIM1_F_1_3: 5′CCTTGTCCATGCAGTCCC	qRT-PCR: This paper	N/A
STIM1_1const_F: 5′CCATGCCAAGGCTAGGCAG	qRT-PCR: This paper	N/A
STIM1_R_2: 5′GCTGCCGCACACTGCTCTG	qRT-PCR: This paper	N/A
STIM1_R_1_2: 5′GGAATGGGTCAAATCCCTCTG	qRT-PCR: This paper	N/A
STIM1_R_3: 5′CTTACTAGAGACGCTGTTTGCC	qRT-PCR: This paper	N/A
STIM1_1const_R: 5′GCCGAGTCAAGAGAGGAGG	qRT-PCR: This paper	N/A
STIM2-F-2-3: 5′CATCGCTAAGGACGAGGCAGA	qRT-PCR: This paper	N/A
STIM2-F-1_new: 5′CTCCTGCAGGCAGAAAAA	qRT-PCR: This paper	N/A
STIM_2const_F: 5′CACTCCCCAGGATAGCAGTT	qRT-PCR: This paper	N/A
STIM2-R-1-2: 5′GAGAGGGCTTTCTTGGCTTC	qRT-PCR: This paper	N/A
STIM2-R-3_new: 5′GGCATCACCACCCAGTTG	qRT-PCR: This paper	N/A

(*Continued on next page*)

Continued

REAGENT or RESOURCE	SOURCE	IDENTIFIER
STIM2-R-1: 5′GGC TTCCAGAATCTTGTGGTC	qRT-PCR: This paper	N/A
STIM_2const_R: 5′TCCTTCATCCAGTTATGAGGTG	qRT-PCR: This paper	N/A
Recombinant DNA		
pMO91_human-STIM1-YFP	Addgene	Plasmid #19754
pEX-YFP-STIM1-deltaK	Addgene	Plasmid #18861
pEX-CMV-SP-STIM2(15–746)	Addgene	Plasmid #18868
pAAV-hSyn-Cre-P2A-dTomato	Addgene	Plasmid #107738
pAAV-Ef1a-mCherry-IRES-Cre	Addgene	Plasmid #55632
ER-GCaMP6-150	Addgene	Plasmid #86918
pAAV Helper	Cell Biolabs	N/A
pAAV2/2	Addgene	Plasmid #104963
AAV-GFP/Cre	Addgene	Plasmid #49056
AAV-CMV-GFP	Addgene	Plasmid #67634
pAAV_hSyn_SP-Halo-STIM1 (23-685aa)	This paper NCBI Ref: NP_003147.2	Based on Plasmid #19754
pAAV_hSyn_SP-Halo-STIM2 (15–746)	This paper NCBI Ref: NP_065911.3	Based on Plasmid #18861
pAAV_hSyn_SP-Halo-TMC	This paper	N/A
pAAV2_hSyn_SP-Halo-STIM1-deltaK (23-670aa)	This Paper NCBI Ref: NP_003147.2	Based on Plasmid #18861
pAAV-Ef1a-mCherry-IRES-CreMut_Y324F	This paper	Modified from Plasmid #55632
pAAV-hSyn-MutCre-P2A-dTomato	This paper	Modified from Plasmid #107738
pAAV_hSyn_synaptophysin-GCaMP6f	This paper NCBI Ref: NM_012664.3	N/A
pAAV_CMV_ER-GCAMP-150	This paper	N/A
pAAV-DJ-6xHis587	This paper	Modified from Koerber et al., 2007
pAAV_CMV_GFP-MAPPER	This paper/Addgene	Modified from Plasmid #117721
Software and algorithms		
ImageJ	NIH	https://imagej.nih.gov/ij/
MetaMorph v7.8.8.0 PalmTracer (Application in MetaMorph)	Molecular Devices Molecular Devices	N/A N/A
NIS-Elements	Nikon	https://www.microscope.healthcare.nikon.com/de_EU/products/software/nis-elements
Leica LAS X Office	Leica-Microscopy	https://www.leica-microsystems.com/products/microscope-software/p/leica-las-x-ls/#downloads
GraphPad Prism v9	GraphPad	https://www.graphpad.com/
Patchmaster	HEKA Elektronik	https://www.heka.com/
Fitmaster	HEKA Elektronik	https://www.heka.com/

EXPERIMENTAL MODEL AND STUDY PARTICIPANT DETAILS

Primary hippocampal neuronal cultures

Primary cell cultures were prepared from the following mouse lines: B6.Cg-Stim1tm1Rao/J (Stim1fl/fl) and B6.Cg-Stim2tm1Rao/J (Stim2fl/fl) ([44]; Jackson Laboratory, strain numbers 023350 and 023351, respectively), GAD67-GFP knock-in mice ([86] and Gt (ROSA)26Sortm1.1(CAG-cas9*,-EGFP)Fezh/J (RRID:IMSR_JAX:024858, Common Name: Rosa26-Cas9 knockin). Dissociated primary hippocampal neurons were obtained from mouse pups (collectively referred to in this study as STIM1, STIM2, Cas9, or GAD67-GFP) housed at the Translational Animal Research Center (TARC) in Mainz. Hippocampi were dissected from postnatal day 0 (P0) mouse pups using both male and female pubs in compliance with European and local animal welfare regulations. The tissue was washed three times with cold HBSS (Sigma, H9394) and incubated with 1× trypsin-EDTA (Gibco 15400-054) for 15 min to facilitate dissociation. Cells were seeded onto poly-L-lysine (Sigma, P1149) coated Ø18 glass coverslips at a density of 70,000 cells

per coverslip in 12-well plates. Neurons were cultured in Neurobasal (Gibco, 12348-017) medium supplemented with 2% B27 (Gibco, 17504044) and 5 mM L-glutamine (Gibco, 25030-024) and maintained at 37°C in a humidified 95% air/5% CO2 incubator.

HEK 293T cell culture

HEK 293T cells (Originally referred to as 293tsA1609*neo* from DSMZ, Ref. ACC 635) were cultured in DMEM (Gibco, 41966-029) supplemented with 10% fetal bovine serum (Thermo, V30160.03) and 1% L-glutamine (Gibco, 25030-024) at 37°C in a humidified 5% CO2 atmosphere and passaged weekly. Cells were maintained in T25 flasks and regularly tested for mycoplasma contamination. For experiments cells were transferred to poly-D-lysine-coated (MERK-Sigma, P1149) Ø18 glass coverslips. For sub-culturing or experiments, cells were briefly washed with HBSS (MERK-Sigma, H9394) and detached using trypsin-EDTA (Gibco 15400-054), then transferred to 12-well plates at a 1:10 dilution.

HEK 293 $Ca_V1.2$ cell culture for electrophysiology

HEK293T cell line stably expressing full-length human $Ca_V1.2$ e[1b/8b/-9*/22/32/33] and auxiliary subunits human $Ca_V\alpha2\delta1$and human $Ca_V\beta3$ [95] were created by Dr. Henning Draheim Boehringer Ingelheim Pharma GmbH & Co. KG CNS Diseases. The cells were cultured in DMEM (Gibco, 41966-029) supplemented with 10% fetal bovine serum (Thermo, V30160.03) and 1% L-glutamine (Gibco, 25030-024) at 37°C, and maintained in selective medium (hygromycin 50 μg/mL, blasticidin 15 μg/mL, geneticin 500 μg/mL) with a humidified atmosphere containing 5% CO2 and 95% air. For cell detachment during experiments or sub-culturing, the cells were initially washed with HBSS (Sigma, H9394) and subsequently detached using Trypsin + 1× EDTA (Gibco, 25300-062) under sterile conditions. Culturing was carried out in T25 flasks, and for electrophysiological experiments, cells were transferred to poly-D-lysine-coated (MERK-Sigma, P1149) Ø18 glass coverslips (12–24 h before experiments). For STIM1 overexpression experiments, the cells were transfected with a plasmid coding for human STIM1 fused with YFP (Addgene, plasmid no. 19754) 3 days before experiments. Expression of $Ca_V1.2$ subunits was triggered by 1 μg/mL doxycycline treatment (applied to the cell medium 2 days prior to experiments).

METHOD DETAILS

Transfection of cell line

HEK 293T cells in 12-well plates were transfected with 1 μg of plasmid DNA using Polyethylenimine PEI (1 mg/mL, Sigma, 408727) at a 1:3 w/v ratio. DNA and PEI were diluted separately in Opti-MEM (Gibco, 31985-070), combined, and incubated for 10 min at RT. A 100 μL DNA-PEI complex was added to 70% confluent cells, followed by gentle swirling. Media was replaced 3–6 h post-transfection, and gene expression was analyzed 48–72 h later.

Transduction of hippocampal neuronal cultures

For transgenic gene delivery, hippocampal neurons were infected with rAAV2 or rAAV DJ-6xHis at DIV 2 for experiments involving Cre recombinase-mediated knockdown or at DIV 7 for the introduction of constructs encoding genes of interest (GOIs) such as STIM1, STIM2, ER-GCaMP-150, synaptophysin-GCaMP6f, PSDfingr, or Mapper. The acquisition and analysis of infected neurons were conducted between DIV 7 and DIV 14 to monitor gene expression and the efficiency of transgene delivery. Prior to using each new viral preparation, infectivity assessments were performed using serial dilution to fine-tune the optimal infection volume, ensuring optimal or a 100% infection rate. For specific experiments, lower infection rates were intentionally applied and are detailed within the respective experiment.

Knockdown of STIMs

To knock-down the expression of STIM1 and STIM2, neuronal cultures set up from Cre/*loxP* mice (JAX strains no 023350 and 023351, respectively) were transduced with AAV-DJ-hSyn-Cre-P2A-TdTomato virus at DIV2. The efficiency of knockdown was determined by performing immunolabeling at DIV 14–16, followed by confocal microscopy. To achieve moderate transduction efficiency that would enable the comparison of naive and knock-down neurons on the same coverslip, low concentration of viral particles was used. The intensity of STIM1 and STIM2 signal in TdTomato-positive and negative neurons was compared. As a negative control, neurons were transduced with viral particles coding for a mutated, inactive Cre recombinase (AAV-DJ-hSyn-ΔCre-P2A-TdTomato).

Generation of CRISPR-Cas9 STIM1/STIM2 knock-ins

STIM1 and STIM2 knock-ins were generated using the pORANGE template vectors, based on the method described by,[45] with modifications to the knock-in cassettes. These cassettes included the U6 promoter, gRNA, and donor DNA (Halotag in this study) but excluded SpCas9. Instead, floxed Cas9 mouse lines were utilized for Cas9 expression. The modified knock-in cassettes were integrated into an rAAV vector and delivered to neuronal cultures at DIV2, along with an rAAV vector carrying Cre recombinase for simultaneous transduction. To ensure minimal impact of the inserted tag sequence on protein function, we carefully analyzed the functional domains of STIM1 and STIM2, including signal peptide presence. The tag was positioned close to or immediately following the signal peptide to preserve protein integrity, similar as in our overexpression constructs. Genomic sequences were obtained

from the UCSC genome browser to identify suitable PAM sites within these regions. Target sequences were selected with attention to the MIT guide specificity score, ensuring precision in genome editing. The sequences chosen were CCCGCGGAGGTGCCGGGGCA for STIM2 and GTATTCTTTTCACTGTGACT for STIM1.

Recombinant DNA

Plasmids DNA used in this study included pMO91_human-STIM1-YFP (Addgene, ref# 19754;[87]), pEX-YFP-STIM1-deltaK (Addgene, ref# 18861; [8]), and pEX-CMV-SP-STIM2(15–746) (Addgene, ref# 18868;[88]). Constructs generated/modified within this study included pAAV_hSyn_SP-Halo-STIM1 (23-685aa) (based on NP_003147.2, NCBI), pAAV_hSyn_SP-Halo-STIM2 (15–746) (NP_065911.3, NCBI), pAAV_hSyn_SP-Halo-TMC, pAAV2_hSyn_SP-Halo-STIM1-deltaK (23-670aa) (NP_003147.2, NCBI), pAAV-Ef1a-mCherry-IRES-CreMut_Y324F, pAAV-hSyn-MutCre-P2A-dTomato, pAAV_hSyn_synaptophysin-GCaMP6f (NM_012664.3), pAAV_CMV_ER-GCAMP-150, pAAV-DJ-6xHis587, and pAAV_CMV_GFP-MAPPER Additionally, the pAAV-hSyn-Cre-P2A-dTomato plasmid was obtained from Addgene (ref# 107738), pAAV-Ef1a-mCherry-IRES-Cre (Addgene, ref# 55632), ER-GCaMP6-150 (Addgene, ref# 86918;[47]), pXX2 (rAAV2-6XHis587), provided by Prof. David V. Schaffer, UC Berkeley,[89] pAAV Helper (Cell Biolabs), pAAV2/2 (Addgene, ref# 104963), AAV-GFP/Cre (Addgene, ref# 49056;[90]), and AAV-CMV-GFP (Addgene, ref# 67634;[91]).

In this work, most constructs utilized an rAAV-based vector backbone with a human synapsin promoter to drive neuron-specific expression. The synthetic rAAV2 backbone containing ITRs was derived from the AAV-CMV-GFP plasmid (Addgene, #67634). For the pAAV_hSyn_SP-Halo-STIM1 (23-685aa) construct, the SP-STIM1 sequence was amplified from Addgene, ref# 19754, while the Halo tag sequence was amplified from the TUBB-5 Halo plasmid (Addgene, #64691). These elements, along with the hSyn promoter and a (GS4)2 flexible linker between the Halo tag and STIM1, were ligated into the rAAV backbone. Similarly, for the pAAV_hSyn_SP-Halo-STIM2 construct, the STIM2 sequence was amplified from Addgene, ref# 18868. For the pAAV_hSyn_SP-Halo-TMC construct, pAAV_hSyn_SP-Halo-STIM1 was used as the template, with the STIM1 sequence removed and the transmembrane (TM) region retained immediately after the Halo tag sequence. This construct, which included the SP (1-23aa) of STIM1 followed by the Halo tag and the STIM1 transmembrane region, served as a Halo tag control. The AAV2_hSyn_SP-Halo-STIM1-deltaK construct was created by amplifying the STIM1-deltaK fragment from Addgene, ref# 18861, and replacing the STIM1 sequence in pAAV_hSyn_SP-Halo-STIM1 with the STIM1-deltaK fragment. For Cre-recombinase control experiments, the pAAV-Ef1a-mCherry-IRES-CreMut_Y324F and pAAV-hSyn-MutCre-P2A-dTomato constructs were generated by inserting the Y324F mutation from pAAV-Ef1a-mCherry-IRES-Cre (Addgene, ref# 55632) into these plasmids, using pAAV-hSyn-Cre-P2A-dTomato (Addgene, ref# 107738) as a reference. The pAAV_CMV_ER-GCAMP-150 construct was created by amplifying the CMV_ER-GCAMP-150 sequence from Addgene, ref# 86918, and inserting it into the rAAV backbone. Lastly, pAAV-DJ-6xHis587 was designed following the method described by Koerber et al., 2007, where a 6-residue histidine tag was inserted at the 587 aa position in the pAAV2-N587X plasmid (Addgene, #130877).

Antibodies and chemicals

Primary antibodies and dyes used in this study were purchased from the following sources: Bassoon (Synaptic Systems, 141 004, 141021), Beta-actin (Synaptic Systems, 251 011), Homer 1 (Synaptic Systems, 160011, 160003), RIM (Synaptic Systems, 140203), Ankyrin-G (Neuromab, N106/36). K_V2.1 (NeuroMab, 75–159), MAP2 (Synaptic Systems, 188011, 188004), NR2B (Alomone Labs, AGC-003), STIM1 (Sigma-Aldrich, S6072), STIM2 (Alomone Labs, ACC-064), and Halo-Tag 646 (Promega, G9281), Fura-2 a.m. (abcam, ab120873), HRP anti-Guinea Pig (Jackson IR, 706-035-148) and HRP anti-Mouse (Jackson IR, 115-035-146)

Pharmacological agents used in this study: DHPG (HelloBio, HB0045), Bicuculline Methiodide (Tocris, 2503), Caffeine (Sigma-Aldrich, C0750), CNQX Disodium Salt (HelloBio/Tocris, HB0204/1045), Cyclopiazonic Acid (CPA) (HelloBio, HB1117), D-AP5/D-APV (HelloBio/Tocris, HB0225/0106), Ifenprodil (HelloBio, HB0339), L-Glutamate (abcam, ab120049), MK 801 Maleate (HelloBio, HB0004), Nimodipine (Tocris, 0600/100), NMDA (N-Methyl-D-Aspartic Acid) (HelloBio, HB0454), Ryanodine (HelloBio, HB1320), and TG (Thapsigargin) (HelloBio, HB1118), Bay K 8644 (Torcis, 1544).

HaloTag labeling

HaloTag labeling was performed using cell-permeable Halo-JF646 (Promega, G9281) ligand. The ligands were prepared as 200 μM stock solutions in water and stored at −20°C in single-use aliquots. For live-cell single-particle tracking, HaloTag ligands were added to the culture medium at a final concentration of 1 nM, and cells were incubated for 30 min to allow labeling before SPT imaging and data acquisition. For fixed staining, 20 nM of the ligand was incubated with cells for 3 h. After incubation, cells were washed twice with neurobasal medium for 5 min each, followed by fixation and permeabilization.

AAV production

A helper virus-free system was used for recombinant adeno-associated virus (rAAV) production. HEK293T cells were cultured to 70% confluency in a T75 flask and transfected with a 1:2 (w/v) plasmid DNA to PEI (1mg/ml) ratio. For transfection, Equimolar amounts of three plasmids (helper, viral coat—either rAAV2 or DJ6xHIS—and the gene of interest) were combined for a total of 30 μg per flask and incubated in 0.9 mL Opti-MEM (Gibco, 31985-070) for 10 min. The transfection mixture was then added to the cells and incubated for 6 h at 37°C with 95% air and 5% CO2, followed by media replacement with fresh DMEM (Gibco, 41966-029) supplemented with 10% fetal bovine serum (Thermo, V30160.03) and 1% L-glutamine (Gibco, 25030-024). After 48 h, cells were scraped and

harvested in 1 mL ice-cold resuspension buffer (50mM Tris; 1M NaCl; 0.001% Pluronic (10%)), subjected to three freeze-thaw cycles, and centrifuged at 13,000g for 15 min at 4°C to separate the crude viral lysate from cell debris. The crude lysate was purified using an iodixanol density gradient and ultracentrifugation. Sequential layers of 15%, 25%, 40%, and 54% iodixanol were added to quick-seal tubes (Beckman Coulter, 342414) containing 7 mL of viral supernatant, then centrifuged at 350,000g for 2 h at 18°C under vacuum. The 40% iodixanol layer containing the virus was carefully extracted, and buffer exchange (1mM $MgCl_2$; 2.5mM KCl; 0.001% Pluronic (10%); pH 7 in 1xPBS) was performed using Amicon ultra-15 filters (100 kDa Millipore, UFC910024), concentrating the volume to 250 μL at 3000 RPM at 4°C. The purified rAAV was stored at −80°C in single-use aliquots.

Western Blotting

Cultured floxed STIM1/STIM2 hippocampal neurons were seeded in 12-well plates and infected at DIV2 or DIV7 with rAAV2 or rAAV DJ-6xHis expressing Cre recombinase to achieve 100% infection (verified through in-lab titration). Cells were harvested at DIV14-16 and lysed in 100 μL SDS sample buffer (62.5 mM Tris-HCl (pH 6.8), 2% SDS, 10% Glycerol, 0.001% Bromophenol Blue, 5% β-Mercaptoethanol) per well, with samples pooled when needed. Protein concentration was measured using the Bradford assay, and 20 μg of protein was denatured at 95°C for 5 min before SDS-PAGE. Proteins were separated on a 10% resolving gel (10% Acrylamide (Rotiphorese Gel 40, Roth, 3030.3), 0.375 M Tris-HCl (pH 8.8), 0.1% SDS, 0.1% Ammonium Persulfate, TEMED) following a 5% stacking gel (5% Acrylamide,0.125 M Tris-HCl (pH 6.8), 0.1% SDS, 0.1% Ammonium Persulfate, TEMED) at 8 mA per gel for stacking and 12 mA per gel for resolving. The PVDF membrane (0.45μM, Roth, T830.1), activated with methanol (Roth, 7342.1), was used for transfer in cold buffer (20% methanol) at 4°C for 3 h at 200 mA. Membranes were washed with TBST (20 mM Tris-HCl, 150 mM NaCl,0.1% Tween 20) and blocked with 5% non-fat milk in TBST for 1 h at room temperature. Primary antibodies (1:1000 in 5% milk TBST, STIM1 (N-Terminal), Sigma-Aldrich, S6072 and STIM2, Alomone labs, ACC-064) were applied overnight at 4°C, followed by three TBST washes. Secondary HRP conjugated antibodies (all from Jackson IR, HRP anti-Guinea Pig, 706-035-148, HRP anti-Mouse, 115-035-146, HRP anti-Rabbit, 711-035-152) (1:2000-1:5000 in 5% milk TBST) were incubated for 1 h, then membranes were washed twice for 10 min each. Protein bands were visualized with HRP substrate (Pierce ECL Western Blotting Substrate, Life Technologies, 32209) following manufacturer protocol using the Intas ChemoStar imaging system (5-min acquisition) and band intensities quantified with ImageJ, normalized to β-actin (Synaptic Systems, 251011) as a loading control.

qRT PCR

Brain tissues (hippocampus, cerebellum, and cortex) were collected from three adult female (3-month-old) STIM1 floxed mice, and up to 100 mg of each tissue was homogenized in 1 mL Trizol (Thermo Fisher, 10296010). After a 5-min incubation at room temperature (RT), 200 μL chloroform: isoamyl alcohol (24:1) (Sigma, C0549) was added, followed by vortexing for 30–60 s. The mixture was incubated at RT for 10–12 min and centrifuged at 12,000g for 15 min at 4°C, and the upper phase containing RNA was collected and mixed with 700 μL isopropanol (Sigma, 190764). After a 10-min incubation at RT (or overnight at −20°C or −80°C for higher RNA yields), RNA was pelleted by centrifugation at 12,000g for 20 min at 4°C, washed with 750 μL 75% ethanol (Sigma, 493546), and air-dried for 15 min. The pellet was resuspended in 30–50 μL RNase-free water (Qiagen, 129114), incubated at 65°C for 5 min, and stored at −80°C. RNA (30 μL) was treated with RNAse inhibitor (NEB, M0314L), DNAse I, RNase-free (1 U/μL) (Thermo Fisher, EN0521) at 37°C for 20–30 min, and purified using the RNeasy Mini spin column (Quigen, 79523). Reverse transcription (with SuperScript III, Invitrogen, 18080051) of 2 μg of RNA was performed in a 20 μL reaction using random/oligo dT primers, incubated at 65°C for 5 min, followed by cooling on ice for 2 min. The remaining RT components were added, and the reaction was incubated at 42°C for 1 h, then heat-inactivated at 80°C for 5 min following manufactures protocol. For qPCR, 10 μL reactions were set up with SYBR Green dye (Life technologies, 4367659) using splice variant-specific primers for STIM1 and STIM2, with each reaction performed in triplicate using the ViiA 7 Real-Time PCR System (Applied Biosystems). Relative quantification (RQ) was determined using the comparative CT method, with RQ calculated as 2(-ΔCT), where ΔCT is the difference between the target gene and housekeeping gene CT values.

Cytosolic Ca^{2+} imaging

Single-cell somatodendritic cytosolic Ca^{2+} levels were quantified using the ratiometric Ca^{2+} indicator, Fura-2-acetoxymethyl ester (Fura-2 a.m., abcam, ab120873). Cultured neurons aged 14–16 DIV were loaded with 2 μM Fura2-AM for 20 min at 37°C in Ringer's solution (NaCl 130 mM, KCl 3 mM, $MgCl_2$ 1 mM, $CaCl_2$ 2 mM, Glucose 10 mM, HEPES 10 mM, pH 7.4, Osmolarity ~310 mOsm.). After washing with Ringer's solution, the cells were left undisturbed for an additional 10 min at 37°C to ensure dye de-esterification and equilibration. Acquisition was performed under the IX71 Olympus microscope equipped with a 40×/1.4NA objective. Fura-2 was excited at 340 and 380 nm with a Polychrome 3000 lamp (Agilent Technologies) and emitted light was captured by an EM-CCD camera iXON Ultra 897 (Andor, pixel size: 16 × 16μm, chip size 8.2 × 8.2mm). Ca^{2+} levels were calculated as the ratio of fluorescence emitted upon 340 nm excitation to fluorescence emitted upon 380nm excitation (peak emission at 510 nm at both excitation wavelengths, excitation filters used: 340/26 and 387/11). Background fluorescence was subtracted, signal calibration was not performed. The intracellular Ca^{2+} levels in individual neurons were measured using MetaMorph imaging software (version 7.8.8.0). Microsoft Excel and GraphPad Prism 9 software were utilized for data processing. For recording basal cytosolic Ca^{2+} levels, neurons were placed in Ringer's solution with 2 mM $CaCl_2$ for 2 min. To evaluate VGCC activity and exclude glial cells from analysis, the PM was depolarized by the application of Ringer's solution containing 50 mM KCl and 10 mM $CaCl_2$ (final concentration). The baseline

was calculated for the first 20 s, and the magnitude of depolarization-induced Ca^{2+} influx was measured as the amplitude following KCl addition.

ER Ca^{2+} imaging

Single-cell somatodendritic ER Ca^{2+} levels were monitored using the genetically encoded probe ER-GCaMP6-210 (Addgene no. 86919), which was delivered via an rAAV2-based vector (AAV-hsyn-ER-GCaMP150) seven days before the experiment. Cultured neurons aged 14–16 DIV were imaged at 37°C in Ringer's solution. Acquisition was performed on the IX71 Olympus microscope equipped with a 40×/1.4NA objective. The fluorescent dye was excited with a Polychrome 3000 lamp (Agilent Technologies) and captured by an EMCCD camera iXON Ultra 897(Andor, pixel size: 16 × 16μm, chip size 8.2 × 8.2mm) using MetaMorph imaging software (version 7.8.8.0). 470/495 excitation and 525/50 emission filters were used. Data processing was conducted using Microsoft Excel and GraphPad Prism 9 software. To assess the magnitude and kinetics of depletion of Ca^{2+} from the ER upon passive leak and NMDAR activation, CPA (HelloBio, HB1117) or NMDA (HelloBio, HB0454) were added at t = 100 s. The magnitude of ER Ca^{2+} efflux was determined as the negative amplitude at t = 400 s, and the kinetics were evaluated by fitting the curve with a single exponential function (between t = 100 s and t = 400 s).

Patch-clamp

Pipettes were pulled with a vertical puller PC-100 (Narishige) from borosilicate glass (Scientific Products, 0.86 mm inner diameter, 1.50 mm outer diameter). Resistance of the pipette tip was between 2 and 5 MΩ when filled with intracellular solution that contained 140 mM CsCl, 3 mM $MgCl_2$, 0.66 mM $CaCl_2$, 10 mM HEPES, 11.7 mM EGTA, 2 mM Na2-ATP, 0.3 mM Na3GTP. Osmolarity was adjusted with sucrose to 300 ± 5 mOsm/kg H2O and pH was set with CsOH to 7.25 ± 5 at room temperature. Extracellular solution contained 140 mM NaCl, 10 mM $BaCl_2$, 10 mM glucose, 10 mM HEPES and 1 mM $MgCl_2$. Osmolarity was adjusted with sucrose to 300 ± 5 mOsm/kg H_2O and pH was set with NaOH to 7.40 ± 5 at room temperature. In ER Ca^{2+} store-depletion experiments, thapsigargin was added to the Ringer solution 10 min before the start of experiments (final concentration 1 μM). In control conditions, DMSO (1:1000 v/v) was used. Recordings were performed at room temperature. After the establishment of the whole-cell mode, the cells were voltage-clamped at −60 mV and access resistance was compensated so that the value did not exceed 5 MOhm. To activate the $Ca_V1.2$ channels, voltage steps from −50 mV to 60 mV were applied every 5 mV. Leak currents have been subtracted online before the channel activation protocol. Signals were acquired with Patchmaster software (HEKA Elektronik), filtered on-line with a 3 kHz low-pass filter, sampled at 20 kHz, amplified by the EPC9 amplifier and digitized with the LIH 8 + 8 AD/DA converter (HEKA Elektronik). Inward current amplitude was quantified (Fitmaster, HEKA), plotted and analyzed for statistical significance (Prism, GraphPad).

Immunolabeling and confocal microscopy

Hippocampal cultures from DIV 14–16 were used for immunolabeling. In a subset of experiments, passive ER Ca^{2+} store-depletion or glutamate stimulation were performed immediately before fixation. The cells were fixed by adding 500 μL of 4% paraformaldehyde (PFA) onto each Ø18 coverslip and incubating for 10 min at 37°C. Next, the 4% PFA solution was removed, and permeabilization was performed by adding 0.5 mL of permeabilization buffer (0.3% Triton in 1xPBS (83 mM Na_2HPO_4, 17 mM NaH_2PO_4, 150 mM NaCl)) for 10 min at RT. Following permeabilization, the coverslips were washed three times for 10 min with washing/blocking buffer that was composed of 2% albumin fraction V (ROTH, CAS no. 9048-46-8), 25 mM glycine, 1× caseine (Sigma-Aldrich, cat. no. B6429) at RT. For immunostaining, coverslips were incubated with primary antibodies targeting the protein of interest diluted in washing/blocking buffer (1:200 dilution) for 4 h at RT or overnight at 4°C, and then washed three times with washing/blocking buffer. Subsequently, coverslips were incubated with secondary antibodies diluted in washing/blocking buffer (1:1000 dilution) for 1 h at RT in the dark and washed again three times. The final washes were performed twice with 1× phosphate-buffered saline (PBS), each for 5 min at RT. Finally, coverslips were mounted with 10μL of Mowiol mounting medium (Roth, 713.2). The mounting medium was allowed to harden overnight at RT in the dark before further analysis. Acquisition of images was performed under Leica Stellaris8 confocal microscope, using 100×1.4 NA oil objective, white light laser and HyD detectors, controlled by LasX software. Pixel size was 60 nm, Z-stacks were acquired with an axial resolution of 200 nm. Images were processed with ImageJ software (NIH).

QUANTIFICATION AND STATISTICAL ANALYSIS

The number of trajectories in SPT experiments, cell culture number (N), number of regions of interest (ROIs, n) and number of cells analyzed for patch experiment are described in the figure legends or related supplementary tables and figures. For comparisons between two groups, a parametric unpaired *t* test was used, while multiple groups were analyzed using one-way ANOVA followed by Tukey's multiple comparisons test. For calculating the significance level GraphPad Prism 9 has been used. Error bars indicate the mean ± SD The significance level is indicated as $^{****}p < 0.0001$, $^{***}p < 0.001$, $^{*}p < 0.1$ within the figures and supplementary tables for figures.

SPT acquisition and analysis

Imaging experiments for SPT of Halo tagged STIMs were performed on a Nikon Eclipse Ti 2 E inverted microscope equipped with an oil immersion TIRF objective (60×, NA 1.45 expanded by 1.5× magnification lens) and the perfect focus system for Z focus

stabilization. Samples were illuminated in TIRF mode, and images were obtained with an exposure time of 50 ms for 500 frames, 20 Hz using an Orca fusion BT sCMOS camera (Orca Flash 4.0 Hamamatsu Photonics, pixel size: 6.5 × 6.5 μm, chip size 13.3 × 13.3 mm). The imaging acquisition was controlled by the NIS Elements advanced research acquisition software (Nikon). During the acquisition, the fluorophores (GFP and Halo tag jenelia 646 were excited by 488 nm and 640 nm at 20% lasers power (Coherent; MPB communications Inc) and a 1.5 × lens in the TIRF coupling was used to illuminate the center of the field of view and to focus the laser power resulting in a pixel size of 0.072 × 0.072 μm^2. The imaging experiments were carried out at 37°C and perfused with Ringer's solution for recordings longer than 5 min to maintain physiological conditions. Acquired image stacks were analyzed using the PALMTracer software package[92] for MetaMorph (version 7.10.3.297). Spots were detected by thresholding the images and localized by fitting a 2D Gaussian function with a 9-pixel radius that matches the microscope's point spread function and an initial sigma of 1.6, achieving ∼40 nm localization accuracy in both x and y dimensions. The average diffusion coefficient (D) for each tracked particle was estimated from the initial MSD versus Δt curve slope (D = MSD/4Δt) using the first 8 time points (50–400 ms).

Workflow of SPT experiment

At DIV 7, Halo-tagged STIMs and synaptic markers were introduced via rAAV infection, with imaging conducted at DIV 14–16. Prior to acquisition, cells were incubated with 646-halo-ligand for 3 h, followed by pharmacological treatment (for test conditions) and washing steps. Imaging was performed in Ringer's solution at 37°C. For single-particle tracking of Halo-tagged STIMs, 500 frames were captured at 20 Hz, while 50 frames were acquired sequentially for the synaptic marker under the same TIRF conditions. Image stacks for both the synaptic label and Halo-tagged STIMs were processed in MetaMorph for ROI selection for localizations. The labeling density, structure of neurites and synaptic labels was taken as signature to select dendritic and axonal compartments. Overlay of dendritic markers with the maximum projections of labeled STIM molecules could allow distinguishing between dendritic and axonal populations of STIMs. An example for the maximum projection is given (Figures S3 and 4N). As indicated in synaptic ROIs (∼160 nm radius, 12 pixels) were marked by briefly aligning the average of synaptic label frames with the maximum projection of 500 SPT frames. Similar size ROIs were placed in the extra-synaptic region for area normalization. Using the same aligned image a cell mask was drawn manually to filter out localizations from axons and dendrites (mapper spots were detected by thresholding the images). Subpixel localizations and trajectory calculations for each region were performed using PALMTracer. To ensure accurate trajectory connections, a maximum fitting radius of 4 pixels (52 nm) between frames was set, based on our visual inspection of fastest moving molecules in our acquisitions. Localizations exceeding this range were excluded as false connections. The diffusion coefficient was calculated from MSD and served as a primary metric for data interpretation across experiments. Diffusion coefficients derived from tracks lasting at least 8 frames (400 ms) were taken in analysis, while shorter tracks were excluded. GraphPad Prism9 was utilized for data visualization, with two types of graphs presented in this study. First, diffusion coefficients were shown as cumulative frequency distributions on a logarithmic scale to pool data from identical conditions. Second, to ensure consistent weighting across experiments, scatterplot of the median diffusion coefficient from each acquisition was plotted and used in subsequent statistical analysis.

Analysis of cluster density and stoichiometry

Analysis of cluster density along dendrites and axons was based on maximum projections of confocal images of neurons either expressing tagged STIMs or tagged endogenous mStims. Background subtraction and maximum projections were performed using build in functions in ImageJ. The use of a Laplacian of Gaussian filter allowed us to define most clusters and allowed to mark them with stereotypic spots. These imposed structures were used to define the density of clusters independent of their individual fluorescent intensity. The axon was initially defined by ankyrin G labeling to distinguish it from thin proximal dendrites (Figure S9). Line scans along dendrites and axons at appropriate line size (between 20 and 30 pixel line width) were used to calculate cluster density.

The stoichiometry of STIMs in individual clusters was estimated on the stepwise bleach of fluorophores inside clusters. The used Halo-ligand JFX 646 has been shown to mainly photo bleach after excitation and to have limited transitions into dark states under physiological conditions.[93] The fluorophore bleaches in a one-step function. After background subtraction 12-pixel ROIs were placed around clusters. The SPT movies were collapsed within an average projection to distinguish clustered from mobile STIMs. In each ROI at least 10 clusters were selected and the bleaching curves analyzed. To reduce the subjective bias, we used an algorithm to verify the individual amplitude of single bleaching steps and back calculate the total number of molecules within the selected region. Image preparation and bleach curves over time were calculated using functions in ImageJ. The cluster calculation was performed using a Phyton-plugin by.[93]